Diploma thesis

Growth morphology of para-hexaphenyl on exfoliated hexagonal boron nitride flakes

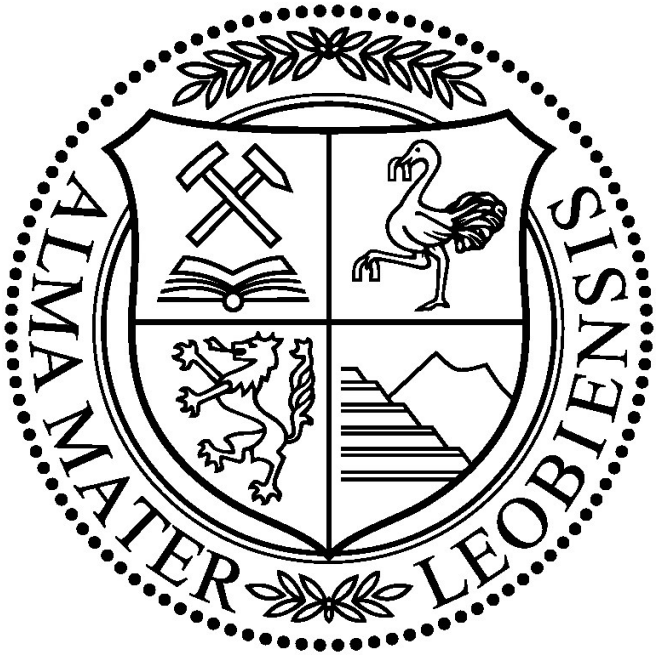

by

Jakob A. Genser

at the Institute of Physics

Montanuniversität Leoben, Austria

under supervision of

Ao. Univ. Prof. Dr. Christian Teichert

Dr. Aleksandar V. Matković

refereed by

Ao. Univ. Prof. Dr. Christian Teichert

Leoben, December 2016

Eidesstattliche Erklärung

Ich erkläre an Eides statt, dass ich diese Arbeit selbstständig verfasst, andere als die angegebenen Quellen und Hilfsmittel nicht benutzt und mich auch sonst keiner unerlaubten Hilfsmittel bedient habe.

Affidavit

I declare in lieu of oath, that I wrote this thesis and performed the associated research myself, using only literature cited in this volume.

_____

Jakob A. Genser

Abstract

Organic semiconductors have been the subject of active research for about a quarter of a century, in the meantime with a number of relevant industrial applications, as energy-efficient lighting, organic and hybrid solar cells, as well as various sensing devices. The most crucial part of every organic field-effect device is the gate dielectric/organic semiconductor interface since it defines charge carrier transport. Interface engineering has been demonstrated to be an effective approach in increasing device quality and performance. Recently, two-dimensional materials have been suggested as a gate dielectric, on which epitaxial grown organic thin films form the active layer. They enable the fabrication of ultra-thin and flexible electronic devices with an atomically smooth and dangling bond free interface due to their van der Waals nature. Among those materials, hexagonal boron nitride (hBN) proved to be one of the most promising candidates for future large-scale industrial applications, since it is capable of sustaining high electric fields, is chemically inert, very flexible, optically transparent, and possible to be produced on a large scale.

This thesis examines the epitaxial growth of the organic semiconductor para hexaphenyl (6P), serving as an example of rod-like conjugated molecules, on top of hBN substrates. High quality, atomically thin hBN flakes, obtained via micromechanical exfoliation, were employed, and the 6P molecules were deposited using hot wall epitaxy. The morphology of the 6P needle-like crystallites was analysed as a function of deposition temperature - ranging from 298-413 K - and hBN substrate thickness using atomic force microscopy. In the temperature range investigated, 6P forms needle-like crystallites, composed of flat-lying molecules, which evolve into networks of long needles only limited by the lateral size of the hBN substrate at elevated growth temperatures. At the same time, the needle density clearly decreases with increasing temperature. The hBN substrate thickness showed to have a major impact on the resulting 6P needle length and degree of ordering. It has been found that a minimal hBN flake thickness of 1.5 nm is necessary, in order to avoid negative effects on the morphology arising from the hBN/SiO_2 interface.

Furthermore, the epitaxial relation between the bulk 6P crystallites and the basal plane of hBN has been investigated. Atomic force microscopy measurement analysis revealed a total of six preferential orientations of 6P needles on top of the hBN substrate. To determine the exact adsorption site of 6P on hBN, the experimentally observed morphology has been compared with density functional theory calculations, which revealed the energetically most favourable adsorption site of individual 6P molecules to lie along the hBN armchair direction, with the centre of the 6P phenyl rings above the nitrogen atoms of the hBN substrate. Therefore, the 6P needle orientations are expected to be along the zigzag directions of the hBN substrate.

The observed deviation of the 6P needle axis by ±5° from these zigzag directions can be explained by the formation of the (-629) contact plane of 6P, previously reported for 6P growth on Cu (110) substrates. The achieved results provide a deeper understanding of the growth and morphology of rod-like organic molecules on the hBN interface.

Kurzfassung

Organische Halbleiter sind seit etwa einem Vierteljahrhundert Gegenstand aktiver Forschung, in der Zwischenzeit mit einer Reihe von relevanten industriellen Anwendungen, wie energie-effiziente Beleuchtung, organische und hybride Solarzellen sowie einer Vielzahl von Sensorvorrichtungen. Der wichtigste Bestandteil jedes organischen Feldeffekttransistors ist die Schnittstelle zwischen Gate-Dielektrikum und organischem Halbleiter, da sie den Ladungsrägertransport definiert. Interface-Engineering hat sich als ein effektiver Ansatz zur Erhöhung der Bauelementqualität und -leistung etabliert. Vor kurzem wurden zweidimensionale Materialien als Gate-Dielektrikum vorgeschlagen, auf denen epitaktisch gewachsene, dünne organische Filme die aktive Schicht bilden. Sie ermöglichen die Herstellung von extrem dünnen und flexiblen elektronischen Bauelementen mit einer atomar glatten und bindungsfreien Schnittstelle, aufgrund ihrer van der Waals-Bindungseigenschaften. Unter diesen Materialien erwies sich hexagonales Bornitrid (hBN) als einer der vielversprechendsten Kandidaten für zukünftige industrielle Großanwendungen, da es einer hohen elektrischen Feldstärke standhalten kann, in großem Maßstab herstellbar, chemisch inert, sehr flexibel und optisch transparent ist.

Diese Arbeit widmet sich der Untersuchung des epitaktischen Wachstums des organischen Halbleiters Para-Hexaphenyl (6P), welcher als Beispiel für stabförmige konjugierte Moleküle dient, auf hBN-Substraten. Hochqualitative, atomar dünne hBN-Flocken, erhalten durch mikromechanisches Exfolieren, wurden eingesetzt, und die 6P-Moleküle wurden mittels Hot-Wall-Epitaxy abgeschieden. Die Morphologie der nadelartigen 6P-Kristallite wurde in Abhängigkeit der Abscheidungstemperatur (293-413 K) und der hBN-Substratdicke mit Hilfe von Rasterkraftmikroskopie analysiert. 6P bildet in dem untersuchten Temperaturbereich nadelförmige Kristallite aus flachliegenden Molekülen, die sich bei erhöhten Wachstumstemperaturen zu Netzwerken aus langen Nadeln formieren, welche nur durch die laterale Größe des hBN-Substrats begrenzt sind. Gleichzeitig verringert sich die Nadeldichte mit steigenden Temperaturen. Die hBN-Substratdicke zeigte einen großen Einfluss auf die resultierende 6P-Nadellänge und deren Ordnungsgrad. Es wurde gefunden, dass eine minimale hBN-Dicke von 1,5 nm erforderlich ist, um negative Auswirkungen auf die Morphologie zu vermeiden, die sich aus der hBN/SiO_2 Grenzfläche ergeben.

Darüber hinaus wurde die epitaktische Beziehung zwischen den 6P-Kristalliten und der Basisebene von hBN untersucht. Die Analyse der Rasterkraftmikroskopie-Aufnahmen ergab insgesamt sechs bevorzugte Orientierungen von 6P-Nadeln auf dem hBN-Substrat. Um die genaue Adsorptionsposition von 6P auf hBN zu bestimmen, wurde die experimentell beobachtete Morphologie mit Dichtefunktionaltheorie-Berechnungen verglichen. Es zeigte

sich, dass die energetisch günstigste Adsorptionslage einzelner 6P Moleküle entlang der hBN „Armchair“-Richtung orientiert ist, wobei die Mitte der Phenylringe über den Stickstoffatomen des hBN-Substrats liegt. Daher werden Nadelwachstumsrichtungen entlang der „Zigzag“-Richtung des hBN-Substrats erwartet. Die beobachtete Abweichung von 6P Nadelorientierungen um ±5° von diesen „Zigzag“-Richtungen kann durch die Bildung der zuvor bereits auf Cu (110)-Substraten gefundenen (-629)-Kontaktebene von 6P erklärt werden. Die erzielten Ergebnisse ermöglichen ein tieferes Verständnis des Wachstums und der Morphologie von stabförmigen organischen Molekülen auf der hBN-Oberfläche.

Acronyms

φ	azimuth
ρ	density
2D	two-dimensional
6P	para-hexaphenyl
AFM	atomic force microscopy
DFT	density functional theory
FET	field effect transistor
FL	few-layer
hBN	hexagonal boron nitride
HWE	hot wall epitaxy
LNA	long needle axis
OFET	organic field effect transistor
OSC	organic semiconductor
R	planar distance
RMS	root mean square
T_D	deposition temperature
t_D	deposition time
vdW	van der Waals

Contents

1. Motivation

Since the Nobel Prize 2010 has been awarded to Andre Geim and Konstantin Novoselov [1] the research on two-dimensional (2D) or van der Waals (vdW) materials has experienced a dramatic upswing [2]. Among those vdW materials, graphene shows the highest thermal and electrical conductivities as well as the best mechanical strength [3]. However, graphene is a conducting material and therefore its applications are limited in some fields [4]. An alternative vdW material, hexagonal boron nitride (hBN) or “white graphene”, also shows remarkable properties in thermal conductivity [5] and mechanical robustness [6]. In addition, it has good chemical stability and is electrically insulating [7-8]. Its unique properties make it a promising material for applications in a variety of applications [9].

Recently, vdW materials have also been proposed to serve as a substrate for the epitaxy of organic molecules [10-16] to be used in organic semiconductor (OSC) devices. For the case of organic field effect transistors (OFETs), they showed to enable a significant enhancement in its performance by optimising the gate dielectric/OSC interface [17-18]. Their interface defines carrier transport, since carriers accumulate at the interface only in the first few molecular layers of the OSC [19-20], and also showed to have a major impact on the device stability [21-24]. The growth of organic molecules proved to be negatively influenced by the gate dielectric´s surface roughness [25], leading to a decrease of carrier transport in OFETs [26]. As a result of the vdW nature of 2D materials, their surface is atomically smooth without dangling bonds or trapped charges at their interface [27]. Therefore, enabling the growth of organic crystallite films with large grains and a low amount of defects [10], allows tuning of carrier transport and performance. hBN, being defect-free, shows great potential as a gate dielectric. Although electrons can tunnel through atomically thin flakes [28], limiting the applications of thin hBN films for field effect transistors (FETs), it enables the use of mono-layer hBN as an encapsulation material for other vdW materials [29-30], preventing the degradation of the encapsulated material upon exposure to ambient conditions [29]. Furthermore, having an almost perfectly matched lattice to graphene [31-32], it can be used to support it, reducing interface roughness, improving stability and electronic properties [33].

The main disadvantage of 2D materials lies in their limited access, due to their complicated and costly manufacturing methods. However, recent advances in epitaxial methods enable the fabrication of high-quality atomically flat hBN thin-films in a substantial amount [34-36]. Combined with the micro-mechanical exfoliation technique for basic research, which has been demonstrated for graphene [1] and other vdW materials [37-38], hBN is a promising material for future large-scale industrial applications.

To study hBN as a vdW dielectric substrate for epitaxially grown of OSC, para-hexaphenyl (6P) was chosen, serving as a well-characterized representative of rod-like conjugated molecules [39-40]. The 6P molecules were deposited on the hBN substrate using hot wall epitaxy (HWE) [41-42], allowing conditions as near as possible to thermodynamic equilibrium with a minimum loss of material. The growth of 6P has already been intensively studied on top of other 2D materials such as graphene [12,16,43-44]. However, unlike graphene hBN consists of two elements reducing its symmetry, therefore, causing a higher corrugation of the substrate surface compared to graphene, potentially strongly affecting the molecular arrangement and diffusion.

In order to study the morphology of the resulting 6P crystallites, atomic force microscopy (AFM) was employed. It provides high-resolution topography images, enabling the exact analysis and characterisation of the hBN samples. In combination with additional examination tools, a better understanding of the epitaxial relations between the 6P crystallites and the hBN (0001) substrate can be obtained. This knowledge should proof to be beneficial for future implementations of 6P, using hBN as a gate dielectric.

2. Theoretical background

2.1. Boron Nitride

This thesis is focused on the hexagonal form of boron nitride, however, it exists in multiple forms that only differ in the arrangement of the boron and nitrogen atoms. There are the non-crystalline amorphous forms of boron nitride, which lack any long-distance regularity in the arrangement of its atoms. Additionally, it has three crystalline structures, hexagonal (hBN), sphalerite (cBN) and wurtzite (wBN) illustrated in Figure 2.1.

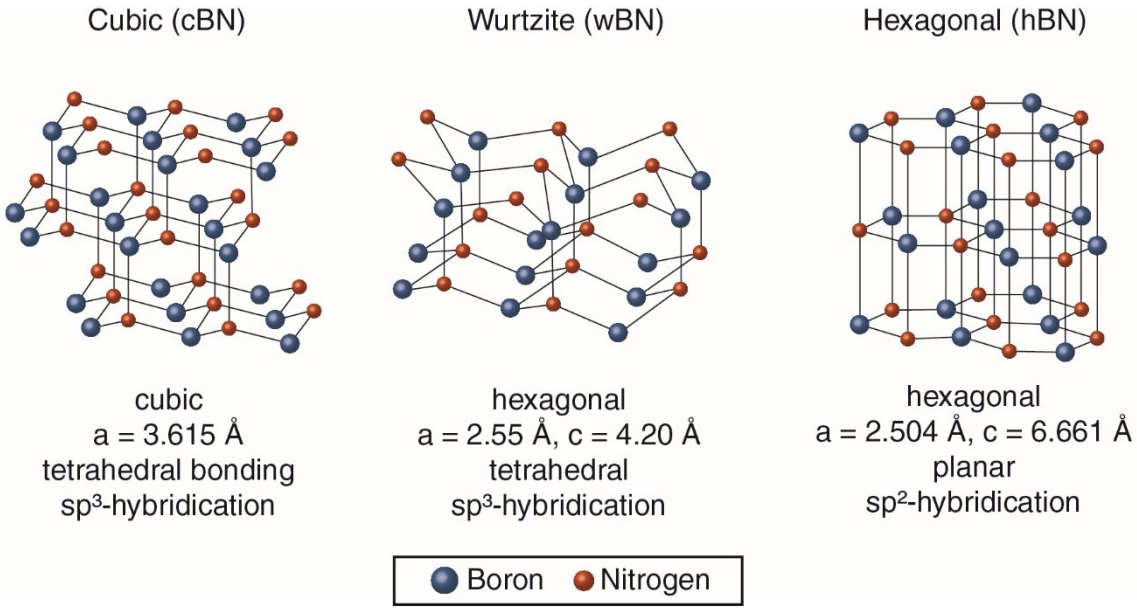

Figure 2.1: Crystalline structures of boron nitride [45].

The cubic boron nitride has a sphalerite crystal structure analogous to that of diamond, being less stable than the hexagonal form. Similar to the sphalerite structure in the wurtzite form of boron nitride, the boron and nitrogen atoms are grouped into tetrahedrons only distinguished by the angles between the neighbouring tetrahedrons. The hexagonal BN is the most stable crystalline form with a high elastic modulus (0.5-0.6 TPa [6]) and a high thermal conductivity (390 W/m · K [7]). It has a layered structure similar to graphite where within each layer boron and nitrogen atoms are bound by covalent bonds. Whereas, the layers are held together by weak vdW forces. The stacking of the layers, on the other hand, differs from graphite since the atoms are eclipsed, with boron atoms lying under and above nitrogen atoms (AA` stacking). Although also other forms of stacking have been observed and analysed the previously described AA` stacking is the most stable one [46]. 2D layers of hBN show high optical transparency in the UV-visible range [47] and their mechanical properties have a dependence on the in-plane stiffness of the films to intrinsic defects present in the films. hBN is relatively inert and expected to have no dangling bonds or trapped surface charges, with a high bandgap

(5.97 eV) resulting from the different on-site energies of the boron and nitrogen atoms [35]. Furthermore, showing a 1.7% lattice mismatch with graphite [48], the atomically planar surface of hBN should be capable of suppressing rippling in graphene [33]. Additionally, the dielectric properties and the surface optical phonon modes of h-BN compare favourable to those of SiO_2 allowing the use of h-BN as an alternative gate dielectric and improving high-temperature and high-electric field performance of hBN based graphene devices [49].

2.2. Para-Hexaphenyl

6P ($C_{36}H_{26}$) consists of six phenyl rings connected by single sp² carbon- carbon bonds forming a rod-like structure with the dimensions 2.66, 0.49 and 0.33 nm (length, wide and height). An illustration of an individual 6P molecule is illustrated in Figure 2.2.

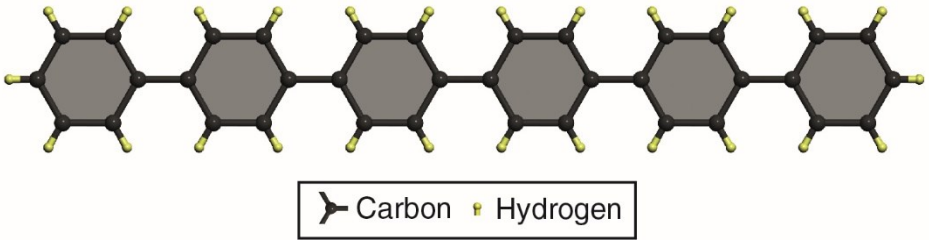

Figure 2.2: Individual 6P molecule

It is a wide-gap OSC with an energy gap of around 3.1 eV [50] and serves as a well-characterized representative of poly(para-phenylene) oligomers [39-40]. Furthermore, it shows high photoluminescence quantum yield in the blue visible range, being a promising material for optoelectronic applications. Moreover, the molecule also can be used as a laser dye [51], for optical waveguides [52], in nonlinear optics [53] and in laser applications [54].

The electronic and optical properties of 6P are highly anisotropic and strongly dependent on the crystal orientation. Therefore, understanding the formation and orientation of the organic crystallites on the substrate is of critical importance in order to enhance the performance of electronic devices. Although phenyl rings are robust building blocks the carbon-carbon bonds connecting the phenyl rings represent the weakest link. This allows the rings to twist and rotate along the molecular axis. Even though, for the crystalline bulk structure averaged molecular planarity can be assumed, meaning that the phenyl rings of a single 6P molecule are arranged in a single plane [55]. The molecules show different growth behaviours depending on their interaction with the substrate. If the configuration with the minimal sample-substrate interaction is favoured island-like crystallites consisting of upright standing molecules are formed, comparable to the Volmer-Weber growth morphology (Figure 2.3 (a), (c)). This can be used for lateral electronic devices. On the contrary, if the configuration with the maximal sample-

substrate interaction is favoured it forms needle-like crystallites consisting out of flat-lying molecules (Figure 2.3 (b), (d)). These needle-like morphologies are of large interest for applications like nano-LEDs, wave guides and lasers.

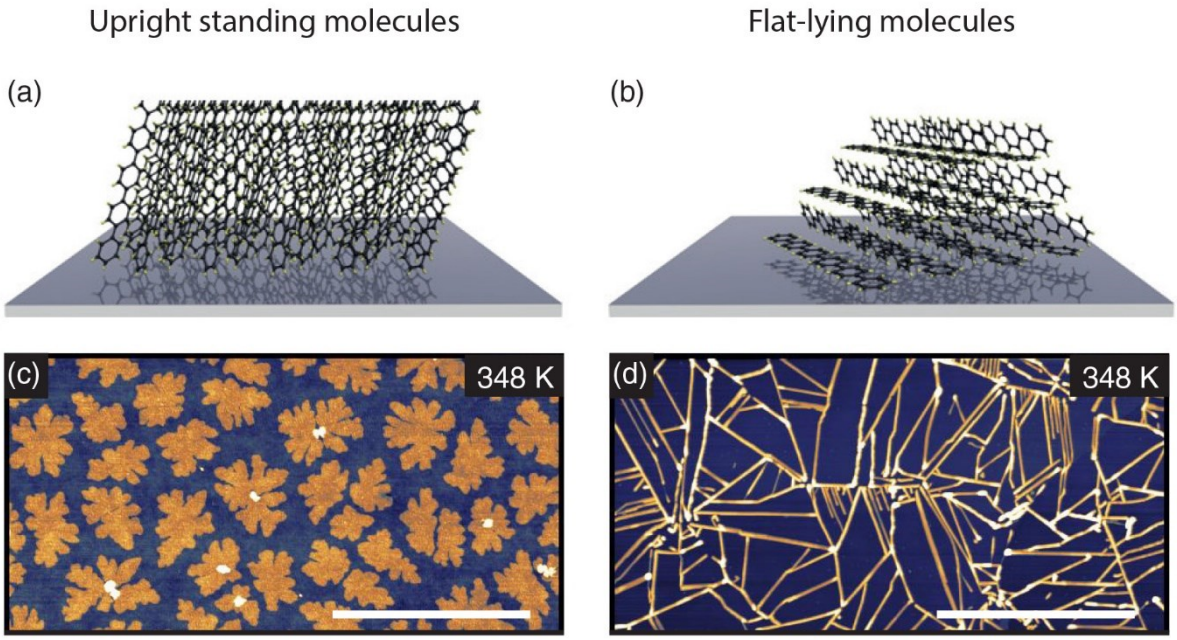

Figure 2.3: Arrangement of the individual 6P molecules (a) for upright standing molecules and (b) flat-lying molecules. (c) Shows the island growth of the 6P crystallites on top a SiO_2 substrate and (b) the needle growth on top of an hBN substrate at a T_D of 348 K (lateral scale bars 4 µm, z scales: 7 nm (c), 15 nm (d)).

The bulk growth of the 6P crystallites achieves the highest energy gain by arranging them within herringbone layers. The crystal bulk structure that is mainly observed is the Baker phase (β-phase), which is a monoclinic crystal, consisting of herringbone layers with the lattice constants a = 8.09 Å, b= 5.56 Å, c = 26.24 Å and β = 98.17° [39]. A unit cell of these layers is highlighted red in Figure 2.4 (b). The long molecular axes of all molecules within the unit cell are oriented parallel to each other whereas adjacent planes are tilted.

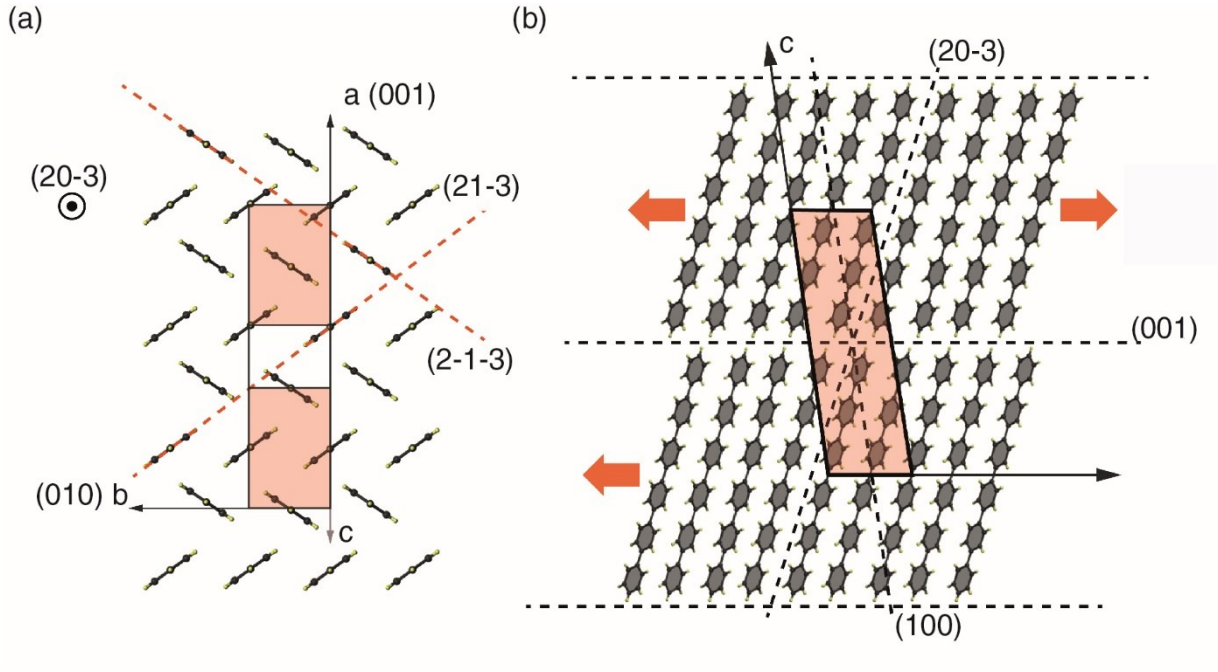

Figure 2.4: Arrangement of the 6P molecules inside the equilibrium Baker phase (a) side view and (b) top view. The red dotted lines in (a) represent the orientation of the tilted 6P molecules and the red arrows in (b) indicate the growth directions of the 6P bulk crystallites. The red highlighted areas represent unit cells of the crystal bulk structure.

2.3. Micromechanical exfoliation

There are several different fabrication techniques to acquire single or few layer hBN films [1,34-38]. For this thesis, the method of choice was micromechanical exfoliation, as a result of being a low-cost fabrication technique giving the best sample quality. However, this method has been mostly used in fundamental research, since it is difficult to scale it up to mass production. hBN needs to be supported by a properly chosen and prepared substrate sticking to the surface through vdW forces. The technique is based on cleavage and uses the property that the vdW forces between hBN and the surface are stronger than the forces between the individual hBN layers. Through an additional cleavage process of the surface, all but the first hBN layer would be removed obtaining a single layer of hBN on the substrate. Micromechanical exfoliation also can be used to prepare thin layers of other materials as graphene, WS_2, WSe_2, MoS_2, and many more [1,37-38]. In addition to the large time investment, there are also other technical issues as it is not possible to directly influence the flake sizes, the number of layers, shape and position on the substrate. To address these issues, it is necessary to prepare a large quantity of samples, using those that seem most promising for growth experiments.

2.4. Hot wall epitaxy

The task for this thesis was to grow epitaxial layers of high crystalline quality. Considering the epitaxial growth, there is a main difference between organic and inorganic materials in their nature of bonds. While inorganic materials are first physisorbed and then chemisorbed on the surface, organic materials form no chemical bonds between the molecules and only physisorption occurs, meaning that the growth process itself is only influenced by weak vdW bonds and Coulomb interactions, which leads to a small sticking coefficient on the substrate. Therefore, the epitaxial growth of organic materials has to be performed at comparable low deposition temperatures (T_D).

Roughly, the deposition techniques for epitaxial layers can be classified into thermal evaporation, cathodic sputtering and chemical deposition. For this thesis, to deposit the 6P molecules, HWE was chosen, a thermal evaporation technique operating in high vacuum. During thermal evaporation, the source material is evaporated with an increase of temperature, which also raises its vapour pressure. The vapour then is channelled towards the substrate where it finally condenses. To ideally deposit a film on the substrate the temperature needs to be high enough for the incident molecules to have sufficient mobility to form a well-ordered structure. Unfortunately, the substrate condition for the condensation of most materials is restricted to comparably low T_D, limited by the reduced sticking probability of the molecules at higher temperatures. The re-evaporation and condensation of incident molecules on cooler parts of the evaporation system can lead to a considerable loss of material. This can be overcome by a large vapour overpressure which usually implies a higher source temperature leading to a growth that takes place under conditions far from thermodynamic equilibrium. However, in the case of vdW epitaxy, it is a specific advantage to work as close as possible to thermodynamic equilibrium. This can be achieved by the setup illustrated in Figure 2.5.

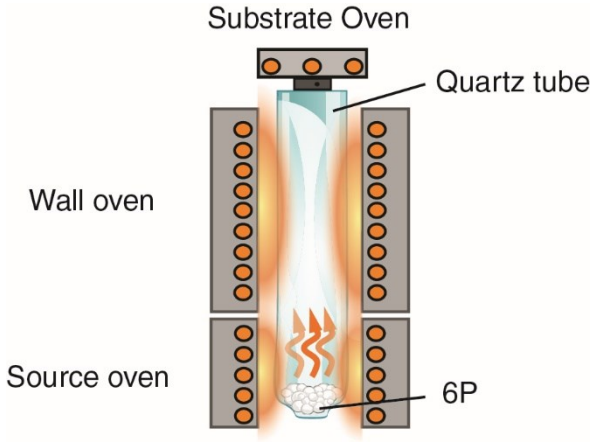

Figure 2.5: Schematic diagram of a hot wall system.

The source material is placed on the bottom of a quartz tube with the substrate sealing off the open end at the top. Three resistance windings heat the substrate, source and wall independently. The whole system is contained within a vacuum and can be considered as a variation of the vapour transport method in a closed tube. This setup leads to a condition as near as possible to thermodynamic equilibrium with a minimum loss of material, since molecules can only condensate at the substrate.

The growth of the epitaxial layers is governed by the evaporation, impingement and deposition rate. By definition the impingement rate of molecules on a surface is the number of molecules which strike the substrate per unit area and per unit time. It can be expressed as a function of the pressure and the temperature of the gas.

$$R_i = \frac{dN_i}{A\,dt} = (2\pi mkT)^{-1/2}\, p \qquad 2.1$$

Where R_i is the impingement rate, N_i the number of incident molecules, A the area of the substrate, m the particle mass, k the Boltzmann constant, T the temperature and p the pressure of the gas. With the help of the Hertz-Knudsen-Langmuir equation, it is also possible to describe the number of molecules evaporating from a surface per unit area and per unit time.

$$R_v = \alpha_v (2\pi mkT)^{-1/2}\,(p_e - p_h) \qquad 2.2$$

R_v is the evaporation rate, α_v is an evaporation coefficient which is dependent on the condition of the surface, T is the surface temperature, p_e the equilibrium pressure of the evaporation material and p_h the hydrostatic pressure on the surface, due to the evaporant in the gas phase. In order to achieve the maximum evaporation rate, you need to obtain the conditions such that $\alpha_v = 1$ and $p_h = 0$. This leads to a simplified equation.

$$R_{v\,max} = (2\pi mkT)^{-1/2}\, p_e \qquad 2.3$$

The condensation of molecules from the vapour phase in order to grow a layer on the substrate is a complicated kinetic process which consists of a series of events. First of all, a fraction of the incident molecules is physically adsorbed, while some of them are immediately reflected. Upon impact, the molecules lose most of their energy and assimilate to the substrate temperature. On the surface, they diffuse until they either are evaporated again or they interact with each other to form a stable nucleus. The film growth starts from these nuclei, which begin to grow by capturing impinging molecules, either from the surrounding surface or directly from the vapour. This nucleation growth is typical for heteroepitaxial growth, the formation of a film of one material on a substrate of a different material [41].

2.5. Atomic force microscopy

In the thesis, AFM [56] was used, in order to resolve nanometre scale features in the sample topography. It can be used for several different applications as imaging, force measurement and manipulation. In force measurements, the forces between the probe and the sample can be measured and applied to perform force spectroscopy investigation. For manipulations, the tip can be used to change the properties of the sample in a controlled way. This thesis only used the imaging capability of the AFM, where a sharp tip at the end of the cantilever is used to scan across the sample surface. Piezoelectric actuators ensure the defined movement of the cantilever. The deflection of the cantilever, caused by the forces between the sample and the tip, are measured by a laser that is directed to the tip of the cantilever, which is reflected to a split photodiode. Alternatively, the measurement of the deflection of the cantilever can be done interferometrically. The deflection of the cantilever gives information about the surface properties of the sample. Simultaneously with the acquiring of the topographical image, further information as stiffness or electrical properties can be obtained [57]. The simplified schematic principle of the AFM is illustrated in Figure 2.6.

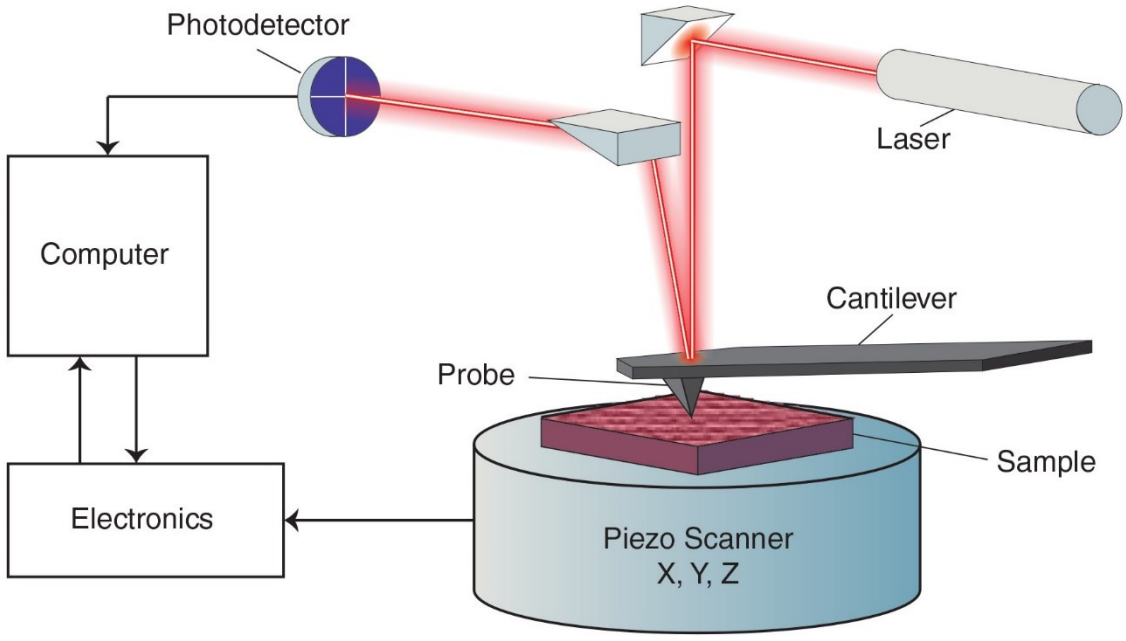

Figure 2.6: Simplified schematic principle of the AFM.

The AFM can be operated in three different principal modes: contact mode, non-contact mode and tapping mode. To obtain the morphology of organic thin films as in this thesis, tapping mode is the method of choice. Tapping mode is a combination of contact and non-contact mode. As in non-contact mode, the cantilever is oscillating near its resonance frequency and

the oscillation amplitude is used as a regulating signal to scan the surface. Although the tip touches the sample, even with higher peak forces than during contact mode, tapping mode generally lessens the damage done to the surface and tip. This can be explained by the short duration of the applied force and the significantly lower lateral forces. This mode is generally used for measurements in ambient conditions.

3. Experimental

3.1. Sample preparation

3.1.1. Micromechanical exfoliation

The micromechanical exfoliation was performed by Dr. A. Matković. One of the most crucial steps to acquire a high quality atomically thin hBN layer is the substrate preparation. In this case, SiO_2 was used as a substrate, which needs to be prepared in several steps. First, any visible dirt needs to be mechanically removed by acetone soaked q-tips and sonication in acetone for several minutes, followed by thermal annealing for about 30 minutes, at temperatures between 200 °C and 250°C. The exfoliation process itself consists of tape preparation, chemical or first exfoliation and mechanical or second exfoliation. In this case, hBN powder was used for the tape preparation and placed between two pieces of a sticky tape. The exfoliation process cleaves the hBN flakes into two pieces, one on each side of the tape. This process is repeated several times until the hBN flakes are thin enough (less than 100 nm) for the chemical exfoliation. The prepared tape is placed over the previously cleaned SiO_2 substrate and put into methyl isobutyl ketone (MIBK) until the tape comes off. The result of this exfoliation is a substrate surface covered with a considerable amount of hBN flakes that are not thicker than a few hundred nanometres. For the mechanical exfoliation, the sample is covered with another tape, which is slowly pulled off. The pulling rate determines the amount, size and thickness of the remaining hBN flakes. Pulling slower will result in larger flakes but will also increase their thickness. If needed, the second exfoliation can be repeated several times. The advantage of this process is that any sample contamination is minimised since the hBN itself is never exposed to any kind of chemicals, tape or tape residue. This consequently results in a sample surface covered with clean flakes of single and few layer hBN [58]. The basic principle of the mechanical or second exfoliation is illustrated in Figure 3.1.

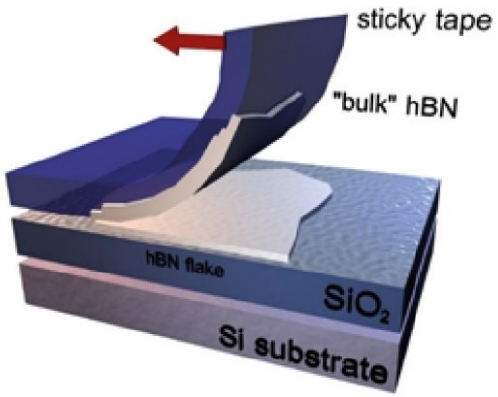

Figure 3.1: Schematic illustration of the micromechanical exfoliation of hBN.

3.1.2. Hot wall epitaxy setup

In order to deposit the 6P molecules on top of the hBN substrate, the previously described HWE method has been applied, allowing conditions as near as possible to thermodynamic equilibrium with a minimum loss of material. To reach the required vacuum of 10^{-6} - 10^{-5} mbar, a diffusion pump combined with an electrically powered rotary oil pump has been used. The source and wall temperatures were fixed at 510 K and 520 K, respectively. Whereas, the sample temperature was varied for different samples from 298 – 413 K. The deposition time for all samples has been set to 300 s, with an approximate deposition rate of (8.8 ± 2.8) 10^{2} molecules/μm^2s. An image of the utilised hot wall system and the exact setup are illustrated in Figure 3.2.

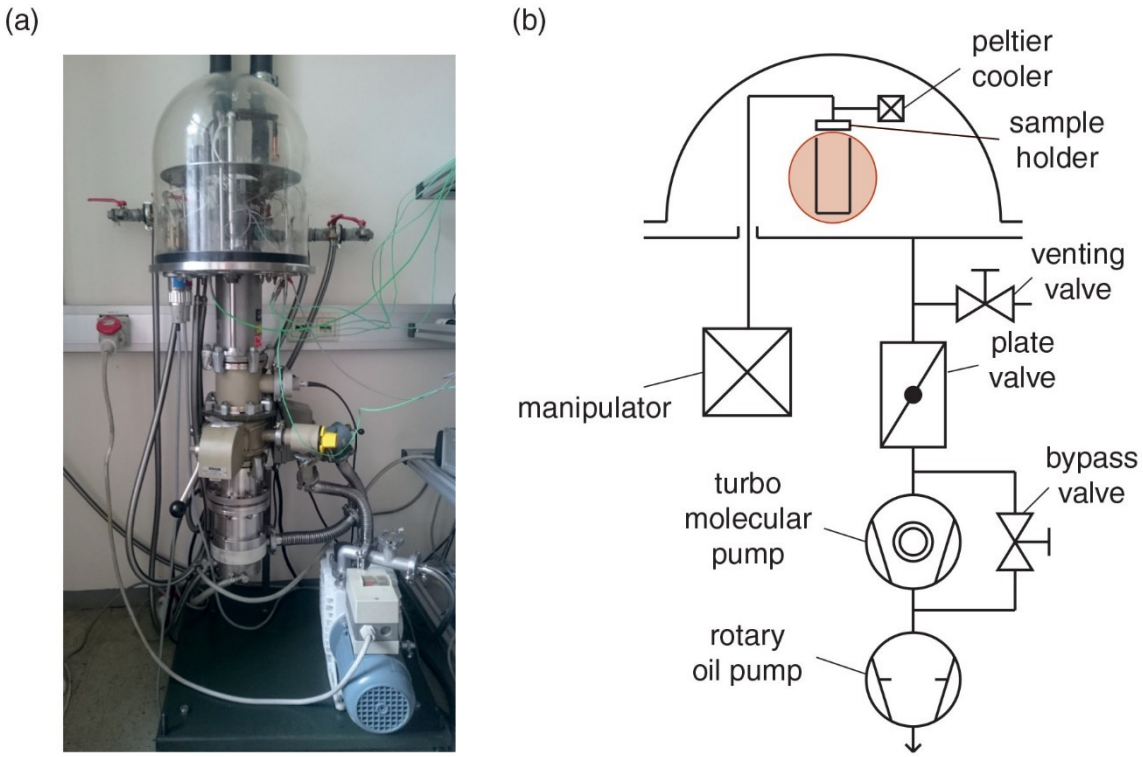

Figure 3.2: (a) Photograph and (b) exact setup of the used the HWE system. The red shaded area in (b) has been illustrated in detail in Figure 2.5.

The 6P molecules, in powder form, are placed inside a quartz tube and installed into the hot wall system. After successfully mounting the hBN sample into the sample holder, the whole system needs to be sealed up and regreased if necessary. After the desired vacuum of about 10^{-6} -10^{-5} mbar is reached the resistance winding heaters are started to heat the substrate, source and wall independently. This leads to a minor increase of the vacuum, due to evaporating residue in the system. Before the deposition process can start, the vacuum needs to reach the desired vacuum again and the substrate, wall and source temperatures have to

be stable. When all criteria are met, the hBN sample is placed on top of the quartz tube sealing it off. The sample might heat up due to the wall oven having a temperature of 520 K. Therefore, depending on the deposition time (t_D) the results might vary by a minor degree, especially for lower T_D. As a counter measure, the samples were cooled during the deposition process, using a Peltier cooler. As soon as the deposition is finished, the sample is taken out of the quartz tube and all heaters are shut off. The vacuum pumps must not be turned off until the temperatures in the system are low enough (about 298 K), to avoid contaminations of the sample and HWE system. When the system cooled down and the HWE chamber has been brought to atmospheric pressure, the sample can be unmounted. All these steps have to be executed with extreme care to not introduce any contaminations into the hot wall system.

3.2. Characterization of the hBN samples

3.2.1. Optical Microscopy

After the micromechanical exfoliation, it is necessary to identify and characterise the mono-, bi-, and few-layer (FL) hBN films. In the case of graphene, they can be identified easily via their optical contrast, using an optical microscope. However, because of its zero opacity, atomically-thin hBN shows little optical contrast on the standard oxide thickness of 300 nm SiO_2, making them undetectable by the human eye. Furthermore, as illustrated in Figure 3.3 (b), at a thickness of 300 nm the contrast changes from positive to negative, going through zero at the region where the eye sensitivity is at its maximum. Therefore, thinner 80 nm SiO_2 was used to optimise the visualisation conditions. At this thickness, the optical contrast for hBN monolayers remains relatively strong with the same sign over nearly the entire visible range. Therefore, it allows to identify hBN mono- and bi-layers under an optical microscope, as shown in Figure 3.3 (b) [47]. The exact classifications of the hBN layer thicknesses will be discussed in the following chapters of this thesis

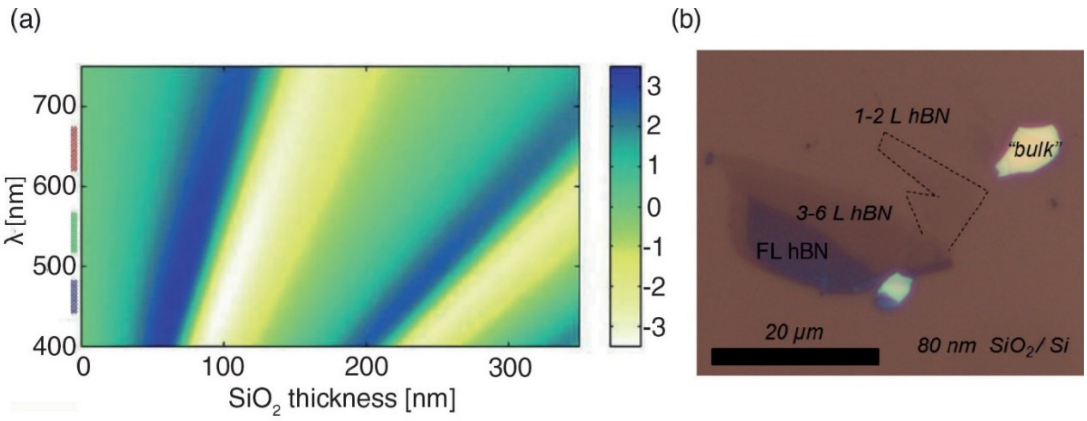

Figure 3.3: (a) Optical contrast due to monolayer hBN for different λ and SiO_2 thickness [47]. (b) Different hBN flake thicknesses on top of an 80 nm SiO_2/Si substrate.

3.2.2. AFM Setup

Further characterization of the hBN samples with and without deposited 6P molecules was performed with the help of AFM measurements. For this thesis, all measurements were implemented by an Asylum Research MFP 3D AFM, illustrated in Figure 3.4. Sensored optical levers with diffraction limited optics and a low coherence light source in the head allows to virtually eliminate interference artefacts. Furthermore, special inductive sensors provide precise measurements of the cantilever position for accurate topography measurements. The corresponding closed-loop scanner uses a flexured scanner, which measures the exact position of each axis. They correct for hysteresis and creep, providing flat scans and the ability to accurately zoom and apply offsets. The entire system operation is controlled through the software interface IGOR Pro.

Figure 3.4: Photograph of the employed Asylum Research MFP 3D AFM.

All measurements were realised in tapping mode under ambient conditions. For further analysis of the data, the free multiplatform modular software Gwyddion [59] was used.

For the topography measurements of the hBN samples, Olympus AC160TS probes were used. Their properties make them optimal for the use in tapping mode under ambient conditions. As illustrated in Figure 3.5 the tip is located at the exact end of the cantilever simplifying the positioning of the laser and the probe. The detailed cantilever and tip specifications are listed in Tables 3.1 and 3.2.

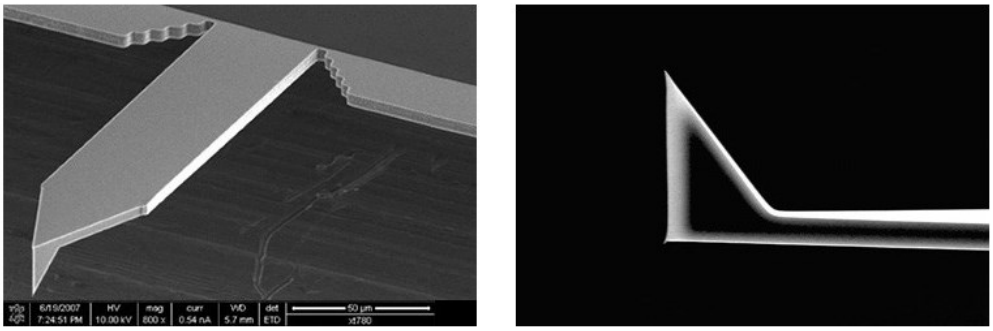

Figure 3.5: Top and side view scanning electron microscopy image of an Olympus AC160TS probe [60].

Table 3.1: Tip specifications of the Olympus AC160TS probe [60].

material	shape	radius [nm]	height [µm]	front angle [°]	back angle [°]	side angle [°]
Si	3-sided	9 ± 2	14 ± 4	0 ± 1	35 ± 1	15 ± 1

Table 3.2: Cantilever specifications of the Olympus AC160TS probe [60].

material	res. freq. [kHz]	spring c [N/m]	length [µm]	width [µm]	thickness [µm]
Si	200 - 400	12 - 103	150 - 170	48 - 52	3.6 - 5.6

4. Results and Discussion

4.1. Identifying mono-layer hBN

Before the 6P molecules were deposited on top of the hBN samples, they were characterised using optical microscopy and AFM. The initial goal was to find as large as possible hBN mono-layer flakes. The optical microscope only allowed a rough estimation of the layer thickness via its optical contrast. Whereas hBN mono- or bi-layers were extremely hard to identify, as seen in Figure 4.1.

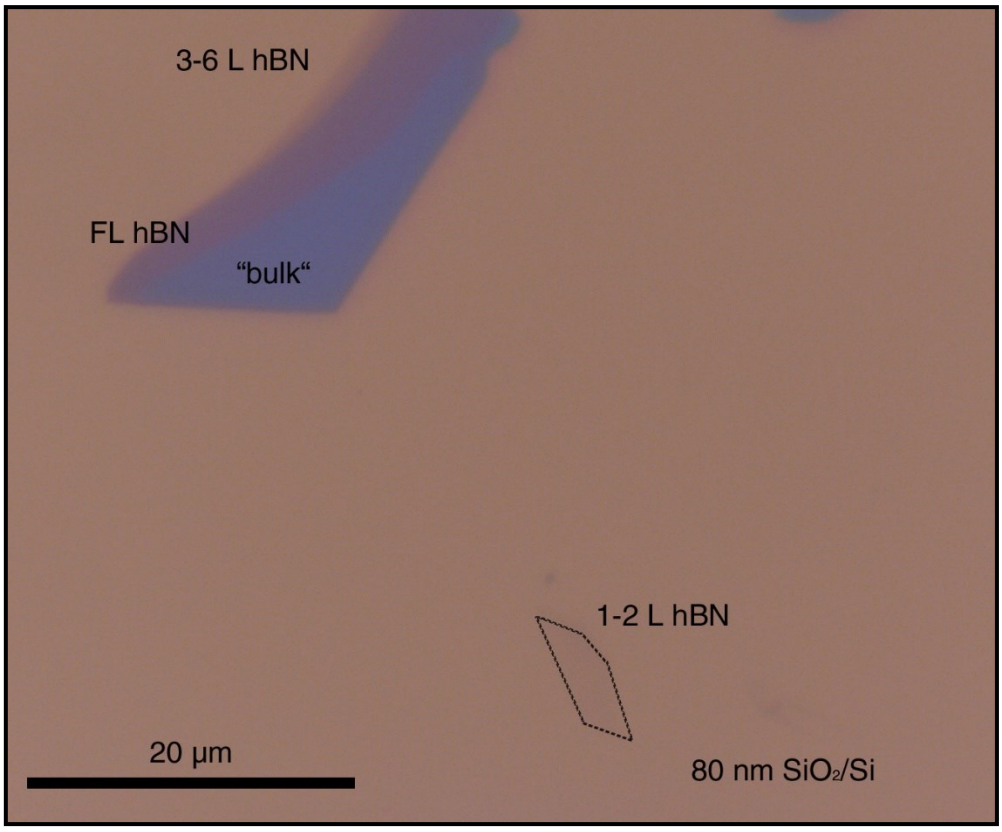

Figure 4.1: Optical image of hBN on top of an 80 nm SiO_2/Siwafer, showing mono-, bi-layer, few-layer (FL hBN) and bulk hBN flakes. The dotted line has been drawn to mark the poorly visible mono- or bi-layer hBN flake.

To determine the exact height and number of layers the suspected mono-layer flake, marked in Figure 4.1, was measured with the AFM. Out of the resulting AFM topographical image, illustrated in Figure 4.2 (a), a one-dimensional height distribution analysis of the red marked area was performed, using the software package Gwyddion. This function is computed as a normalised histogram of the height. The normalisation of the densities ρ (h), where h is the height, is such that

$$\int_{-\infty}^{\infty} \rho(h)dh = 1 \qquad 4.1$$

Therefore, the scale of the values is independent of the number of data points and histogram buckets, resulting in values for the densities out of an interval [0, 1] [61]. Furthermore, the data points were fitted with a multipeak Gaussian fit, resulting in the height distribution seen in Figure 4.2 (b). The first peak resembles the height of the SiO_2 substrate and the second peak the height of the hBN flake. The peak-to-peak distance gives a good estimation of the thickness of the hBN flake.

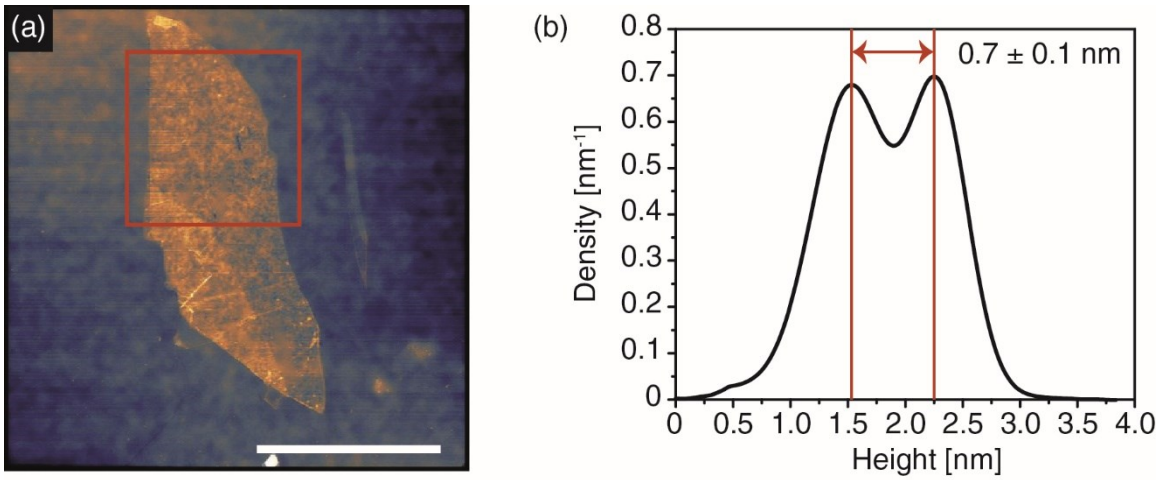

Figure 4.2: (a) AFM topographical image of a suspected mono-layer hBN flake on top of an 80 nm SiO_2/Si substrate (lateral scale bar 4 µm, z scale: 3 nm). (b) One-dimensional height distribution analysis of the red marked area in (a).

In this case, the thickness of the hBN flake was approximately 0.7 ± 0.1 nm. To estimate the number of layers several parameters have to be taken into account. First of all, the absorption height between two layers of hBN is about 3.3 Å [45]. Furthermore, since hBN is deposited by mechanical exfoliation, it is suspected that there is a water layer trapped between the hBN flake and the underlying SiO_2 [62-63]. Additionally, the change from the attractive regime on the substrate background to the repulsive regime on the sample of the probe might result in slight changes of the resulting measured height, which cannot be ignored measuring in the Angstrom regime [64]. Therefore, it is not fair to claim the exact number of layers, especially for very thin hBN flakes. Nevertheless, it can be assumed that hBN flakes with the height of below 1.5 nm have no more than one or two layers. For thicker hBN films it can be estimated that every three layers of hBN add approximately 1 nm of height to the flake. At a certain thickness of about ten layers, the flakes were referred to as bulk hBN and flakes between 3-10 layers as FL hBN. In general, thinner layers of hBN were not only harder to detect because of its weak contrast in the optical microscope but also because they were significantly smaller

than multi-layer hBN, resulting from the mechanical exfoliation process. Nonetheless, it was possible to identify several suspected mono-layer flakes for further analysis using this method, thereby, proofing that the mechanical exfoliation worked successfully.

4.2. Growth behaviour of 6P on top of hBN

4.2.1. General growth of 6P on hBN

To study the growth of 6P on top of the hBN samples, at first a temperature of 293 K was chosen. Several hBN flakes on the sample were measured and the most representative one was chosen for display. Furthermore, the growth of 6P on top of the SiO_2 substrate was investigated as a comparison to previous results [65].

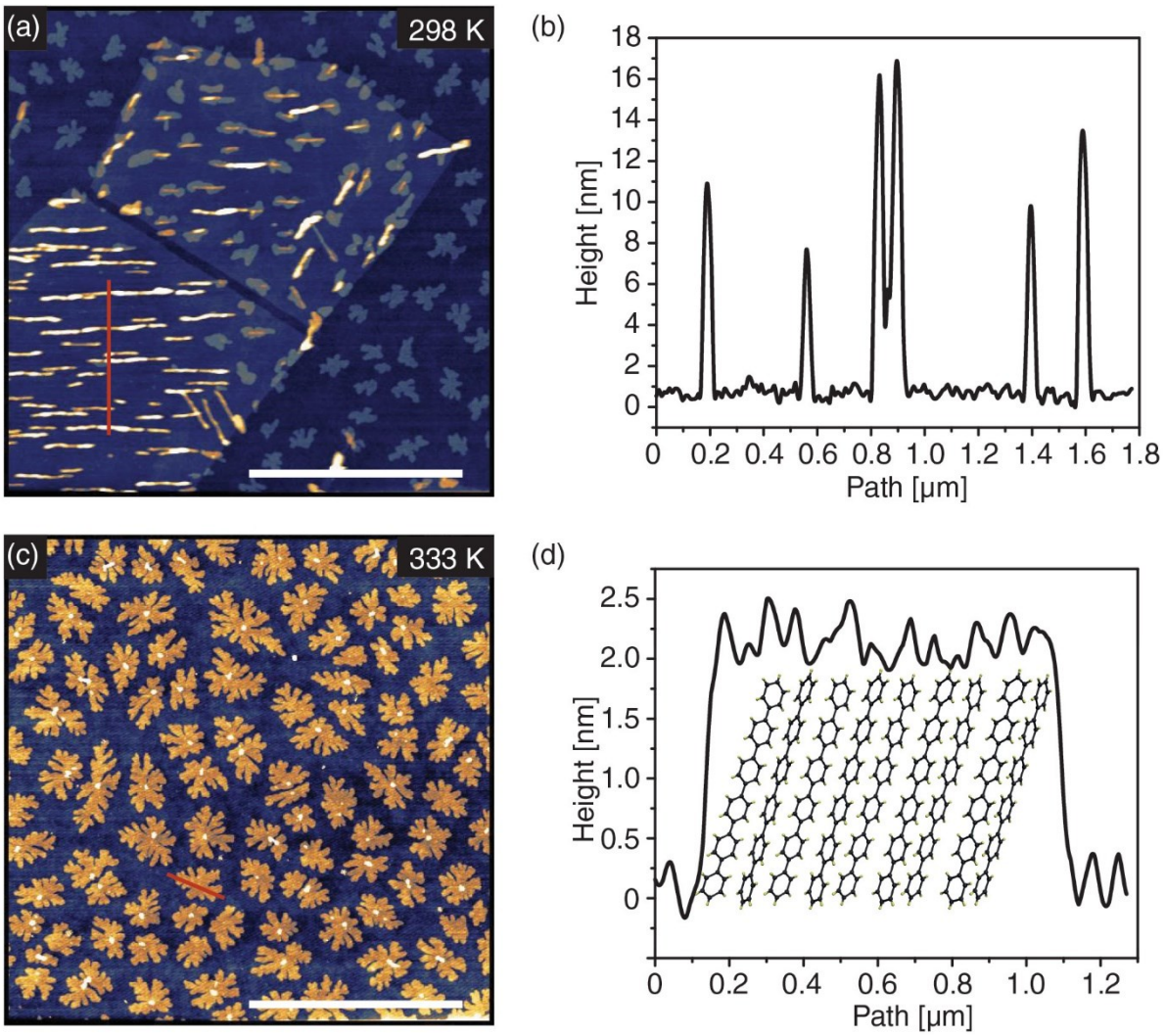

Figure 4.3: (a) A 5 x 5 µm² AFM image of 6P grown on top of an hBN flake at T_D of 293 K. (b) Height profile across 6P needles. (c) A 10 x 10 µm² AFM image of 6P grown on top of SiO_2 at a T_D of 333 K. (d) Height profile across a 6P island consisting of upright standing molecules. Lateral scale bars: 2 µm (a), 4 µm (c), z scales: 20 nm (a), 5 nm (c).

As seen in Figure 4.3 (a), the 6P molecule shows needle-like growth on top of the hBN flake, consisting of flat-lying molecules maximising the sample-substrate interaction. This has also been observed on other substrates with a similar structure to hBN, as for example, graphene [12,16,43-44], mica (001) [66] and KCl (100) [67]. These needles reach a height of several nanometres, displayed in the height profile in Figure 4.3 (b). Furthermore, they seem to show preferential growth directions which will be addressed later in this thesis.

In comparison, Figure 4.3 (c) shows the growth of 6P on top of SiO_2 at a T_D of 333 K. On SiO_2, the 6P molecules show to form island-like structures, consisting of upright standing molecules minimising the sample-substrate interaction. The islands show a height of approximately 2.2 nm resulting from a slight tilt of the 6P molecules illustrated in Figure 4.3 (d), which is in good agreement with literature [68]. Therefore, it can be assumed that there were no inconsistencies during the growth process in the HWE and all results are representative.

4.2.2. 6P overgrowing of edges between hBN terraces

6P needles were found to grow undisturbed over hBN terrace edges on multilayer and bulk hBN flakes. Figure 4.4 shows an example of 6P needles overgrowing hBN terrace edges having heights corresponding to around 15 and 40 hBN layers, at a T_D of 363 K. On top of all samples, it was observed that as long as the 6P needle height is comparable to the height of the hBN terrace the needles tend to overgrow the corresponding edges undisturbed. It is worth mentioning that hBN flakes obtained by mechanical exfoliation are most likely to have the same crystallographic orientation across the entire flake independent of actual thickness. Furthermore, the flake terrace edges usually follow high-symmetry directions of hBN. Additionally, 6P islands on top of the SiO_2 were observed to overgrow the edges of thin hBN flakes, which is in contrast to graphene where the island growth is always stopped at the flake edges [44]. In rare cases, 6P needles also grew from the hBN flakes onto 6P islands on the SiO_2 substrate for a limited distance, ultimately merging into the 6P islands (see Figure 4.3 (a)).

The fact that 6P crystallites can overgrow terraces and flake edges could be beneficial for future large-scale integration of OSC and vdW dielectrics. As indicated from these results, minor defects as cracks or terraces, that usually accompany multi-layer hBN obtained by chemical vapour deposition [34], might not terminate the growth of organic molecule crystallites.

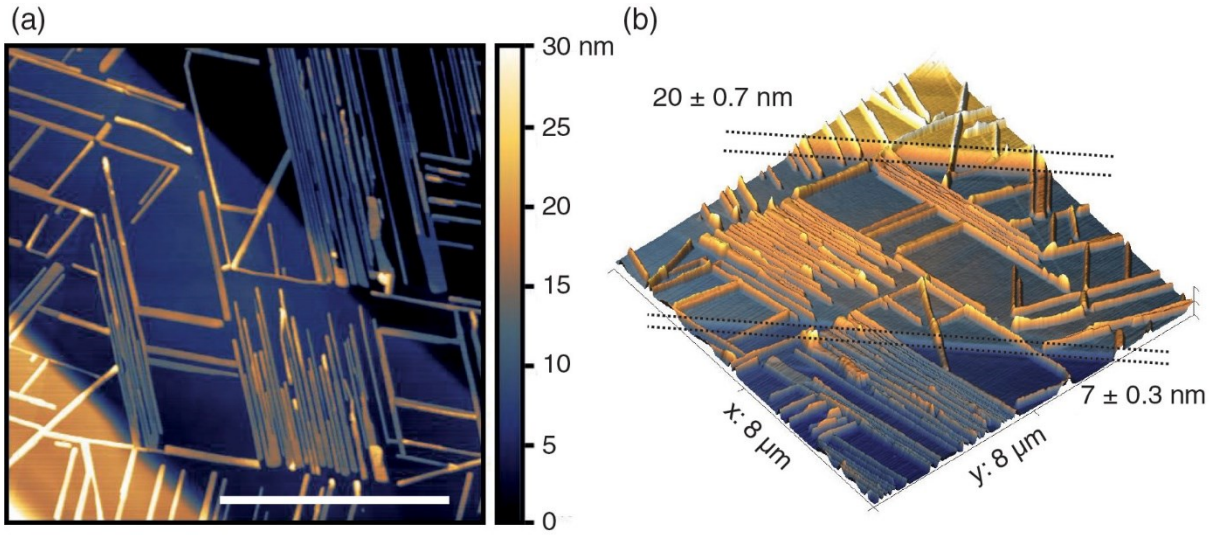

Figure 4.4: 8 x 8 µm² topographical AFM (a) and 3D image (b) of 6P crystallites continuously overgrowing hBN flake edges and terraces on an hBN substrate at T_D of 363 K (lateral scale bar 4 µm, z scale: 30 nm), The thickness of each hBN step is denoted next to the dotted black lines, respectively .

4.3. Influence of the deposition temperature of 6P

A change in T_D revealed a major impact on the resulting growth morphology of 6P crystallites for other similar vdW substrates, such as graphene [44] and mica [69]. Therefore, to study its influence on the growth of 6P molecules on top of hBN, 6P was grown on several previously characterised samples at a T_D range of 298 - 413 K.

The initial intent of this growth experiment was to focus on hBN flakes with a height of no more than 1.5 nm, since as thin as possible layers seem most promising for application in 2D materials, allowing high flexibility of the substrate. On top of the hBN flakes, 6P could be observed to form island as well as needle-like crystallites. However, the overwhelming majority of 6P growth features were needle-like crystallites, and therefore, the focal point was on their investigation. They were analysed according to the general growth morphology, needle length, needle height and total volume per unit area.

4.3.1. Effects on the morphology of 6P

Figure 4.5 and 4.6 show 10 x 10 µm² topography AFM images of hBN flakes with a height below 1.5 nm, covered with 6P needles grown at different T_D between 298-413 K. The T_D shows a significant effect on the growth behaviour and the resulting morphology of 6P crystallites on hBN. By increasing the T_D, the deposited molecules have a higher energy and hence the diffusion of the molecules on the surface is increased. Furthermore, it results in a

reduced nucleation density [70] leading to larger single crystal grains and therefore, reducing the number of grain boundaries per unit area. As a result, with increasing T_D the average length of the needles increases as will be presented later.

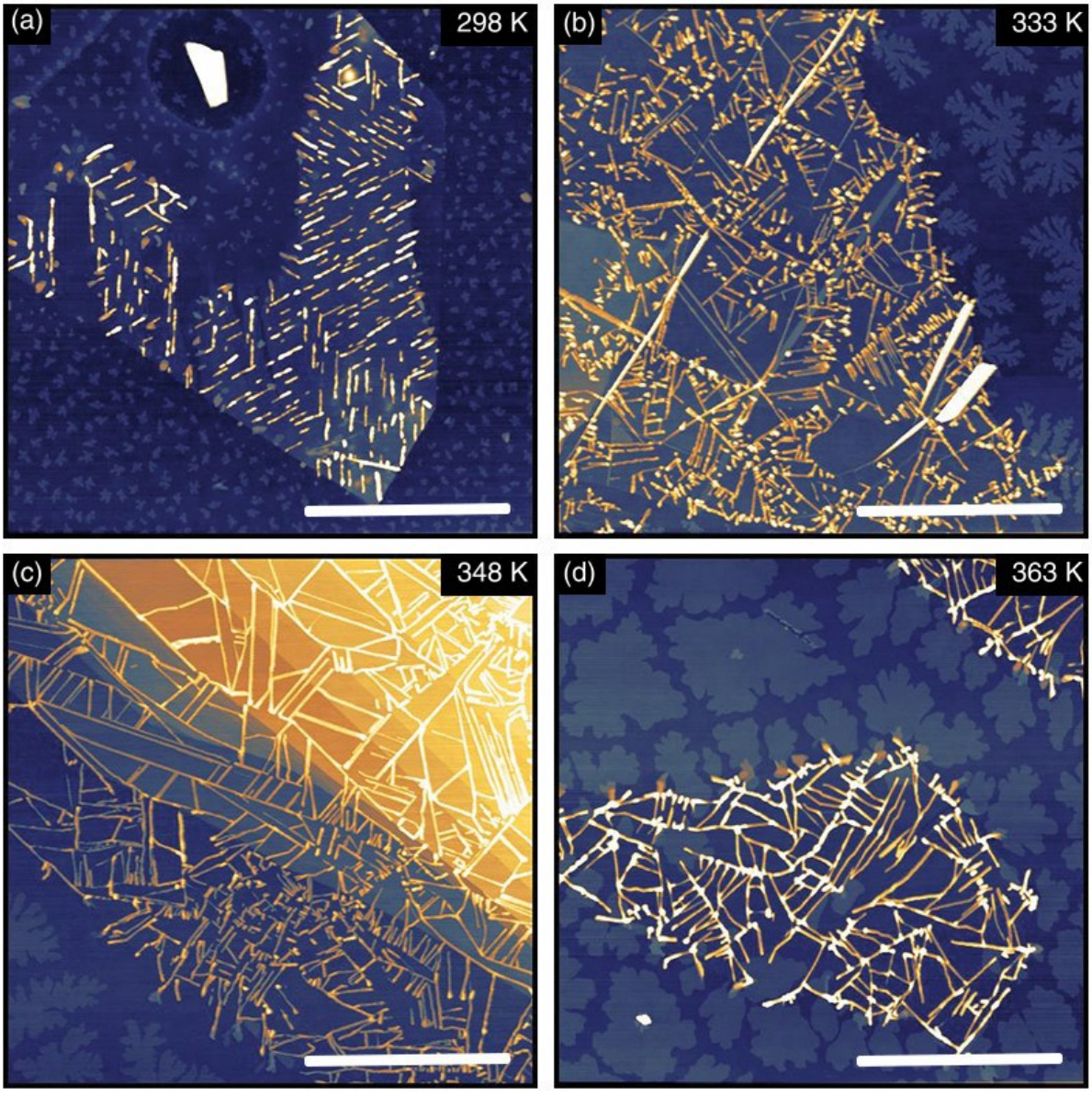

Figure 4.5: (a-d) 10 x 10 µm² AFM topography images, showing the dependence of the 6P morphology with increasing T_D. All images illustrate hBN flakes with a height below 1.5 nm. The only exception is (c), which also has adjacent bulk hBN areas. Lateral scale bars 4 µm, z scales: 20 nm (a, d), 25 nm (b), 45 nm (c). The very high and broad features in (b) are no 6P needles but wrinkles of the hBN flake.

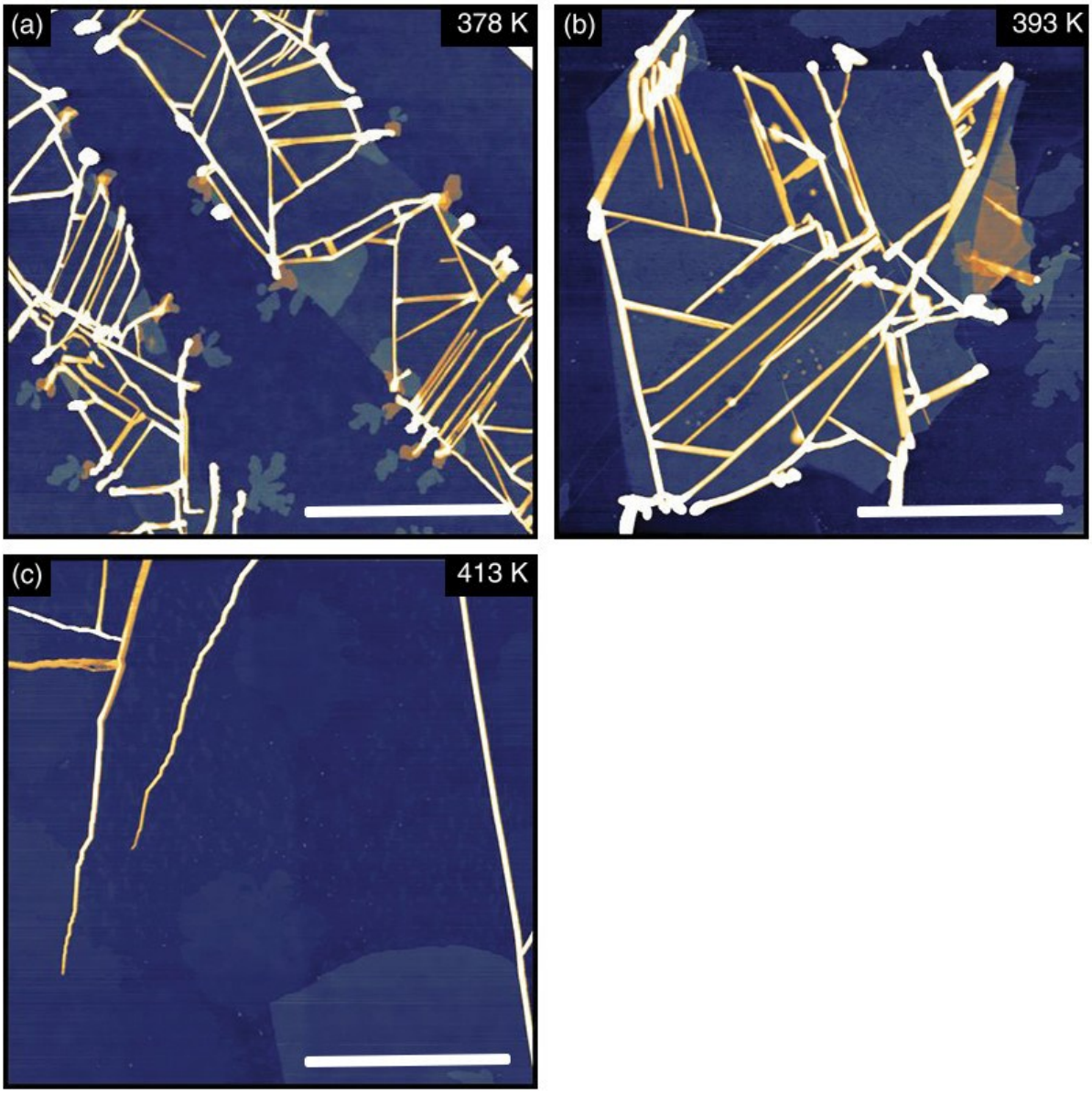

Figure 4.6: (a-c) 10 x 10 µm² AFM topography images, showing the dependence of the 6P morphology with increasing T_D (lateral scale bars 4 µm, z scales: 25 nm (a,), 30 nm (b, c)). At 378 K (a) and 393 K (b), the hBN flakes had a height of below 1.5 nm. At 413 K (c) only bulk hBN was found.

At a T_D of 413 K, there was only a small amount of long needle-like crystallites of 6P left on top of the hBN flakes, indicating that the maximum T_D for the sticking of the 6P molecules is almost reached. Interestingly, at this T_D the 6P needles were able to rapidly change their growth direction, resulting in several needles with staircase-like features (Figure 4.6 (c)).

While analysing the exact length distribution of the 6P needles, it was discovered that there seems to be a major difference between the growth on top of hBN flakes below 1.5 nm and on

top of bulk hBN. This effect is even more noticeable at higher T_D (above 350 K) when the 6P needles grow significantly longer in length. Figure 4.7 shows two 20 x 20 µm² AFM topography images at a T_D of 363 K for an hBN flake with a thickness below 1.5 nm (a) and bulk hBN (b). Not only is there a distinguishable difference in the length of the 6P needles but they also grow in a much more ordered fashion on top of bulk hBN compared to mono- or bi-layer hBN. Therefore, according to the 6P average needle length at different T_D, it was differentiated between hBN flakes that are less than 1.5 nm thick and bulk hBN flakes. Here, bulk hBN flakes are understood to be thicker than 3 nm, measured by AFM. The hBN thickness effects on the morphology of 6P crystallites and their origin will be discussed in detail in later chapters of this thesis.

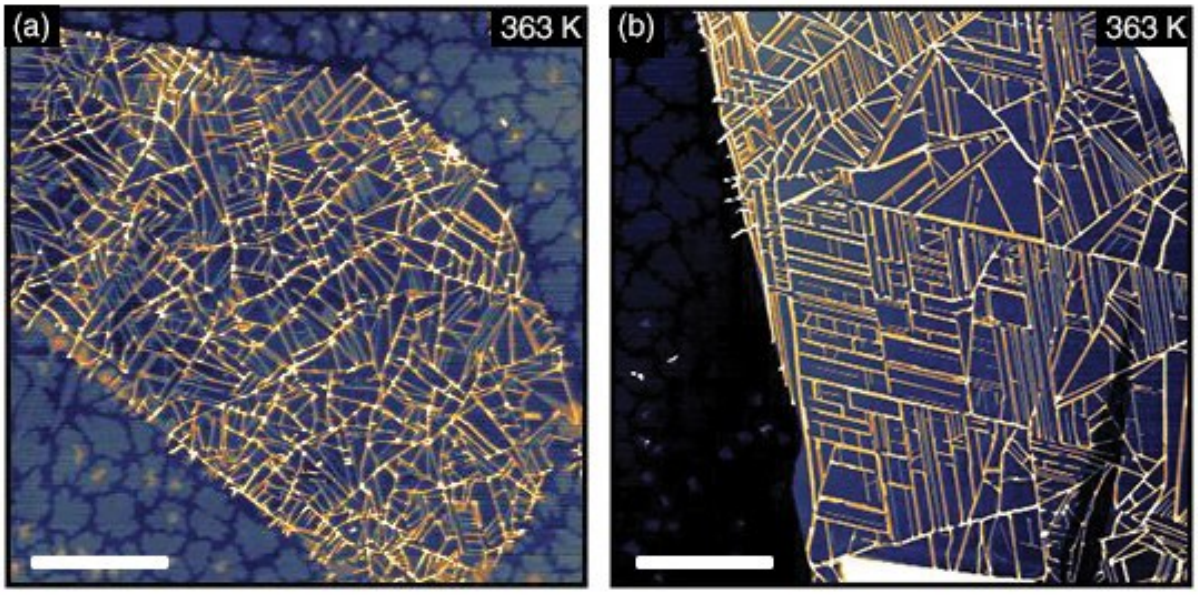

Figure 4.7: 20 x 20 µm² AFM topography images at a T_D of 363 K showing the dependence of the 6P needle growth depending on the hBN flake thickness below 1.5 nm (a) and for bulk hBN (b) (lateral scale bars 5 µm, z scales: 5 nm (a), 50 nm (b)).

To analyse the average 6P needle length, the distance tool provided by the software package Gwyddion was used. It displays the horizontal (Δx), vertical (Δy) and total planar (R) distances, the azimuth φ and the endpoint value difference Δz for a set of lines selected on the AFM image [61]. Since only planar areas where analysed and since 6P needles that overgrew edges were not taken into account, the only relevant value concerning the average 6P needle length was the total planar distance (R).

Figure 4.8 summarises the evolution of the average 6P needle length depending on the T_D and the hBN substrate thickness. Each data point was obtained as an average of more than 400 measured 6P needles including several flakes. As expected, the average 6P needle length increases with rising T_D, however, the effect is significantly smaller for thinner hBN flakes

(below 1.5 nm). Whereas at room temperature (293 K) 6P forms very short needles with an average needle length of below 1 µm, at higher T_D above 393 K, the average needle length is increased to values of almost a magnitude higher. While the average needle length was not found to extend a length of about 5 µm, it does not indicate that individual needles cannot surpass that value by a large amount. At T_D over 380 K, on bulk hBN, several needles were found growing to lengths well over 30 µm. At those T_D the main limiting factor for the needle length was the size of the hBN flakes. The reason why the average value of the needle length at higher T_D is reduced is due to side branches of short needles adjacent to longer ones. These adjacent needles usually do not extend in lengths beyond a few micrometres.

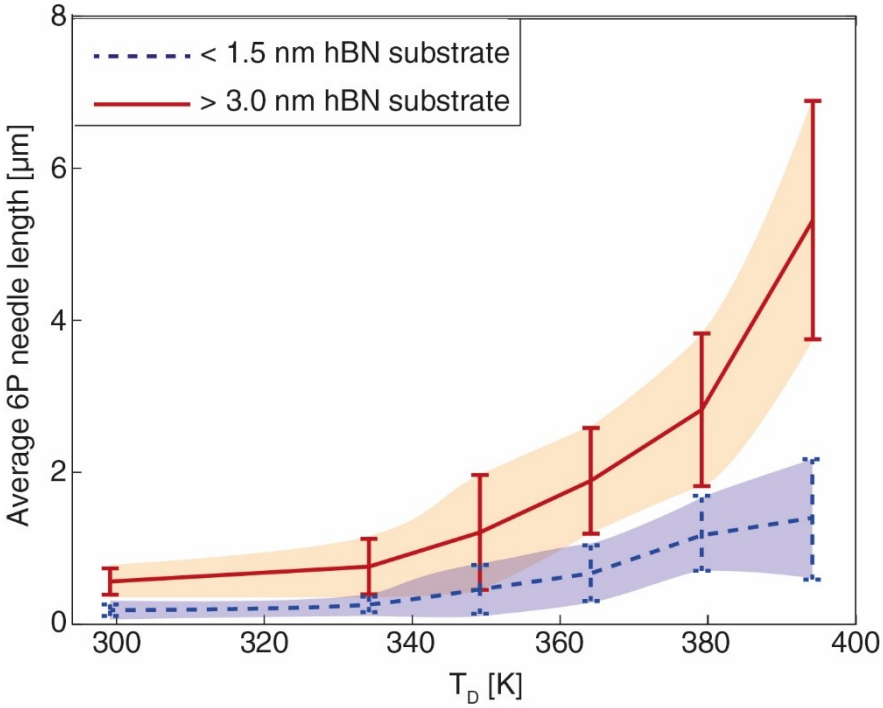

Figure 4.8: Average length of 6P needles as a function of T_D. The solid red line shows the data for 6P needles grown on top of bulk hBN flakes (over 3 nm thick) and the blue dashed line the data for 6P needles grown on hBN flakes with a thickness below 1.5 nm. The shaded areas indicate the standard deviations.

In order to analyse the average needle height of the 6P needles, the profile extraction tool, provided by Gwyddion, was used. The profile curve is constructed from data sampled at regular intervals along the selected line on top of the AFM image [61]. As reference, always the highest point of each needle was taken into account.

Figure 4.9 (a-b) illustrates the dependence of the average 6P needle height on the T_D. Since, according to the needle length, the 6P growth was influenced by the hBN substrate thickness it again was differentiated between thin hBN flakes (below 1.5 nm) and bulk hBN flakes. For every data point, more than 100 needle heights on different flakes were measured. There is only a meagre influence on the average 6P needle height, which is increasing just slightly with

raising T_D. Furthermore, also the hBN substrate thickness shows no major impact on the average 6P needle height, although the needles tend to grow marginally taller on hBN bulk flakes. Concerning the average 6P needle height, the main growth parameter showed to be the t_D (illustrated in Figure 4.9 (c)). With increasing t_D, the amount of 6P needles does not rise significantly but the 6P molecules rather tend to attach to already existing needles increasing their height.

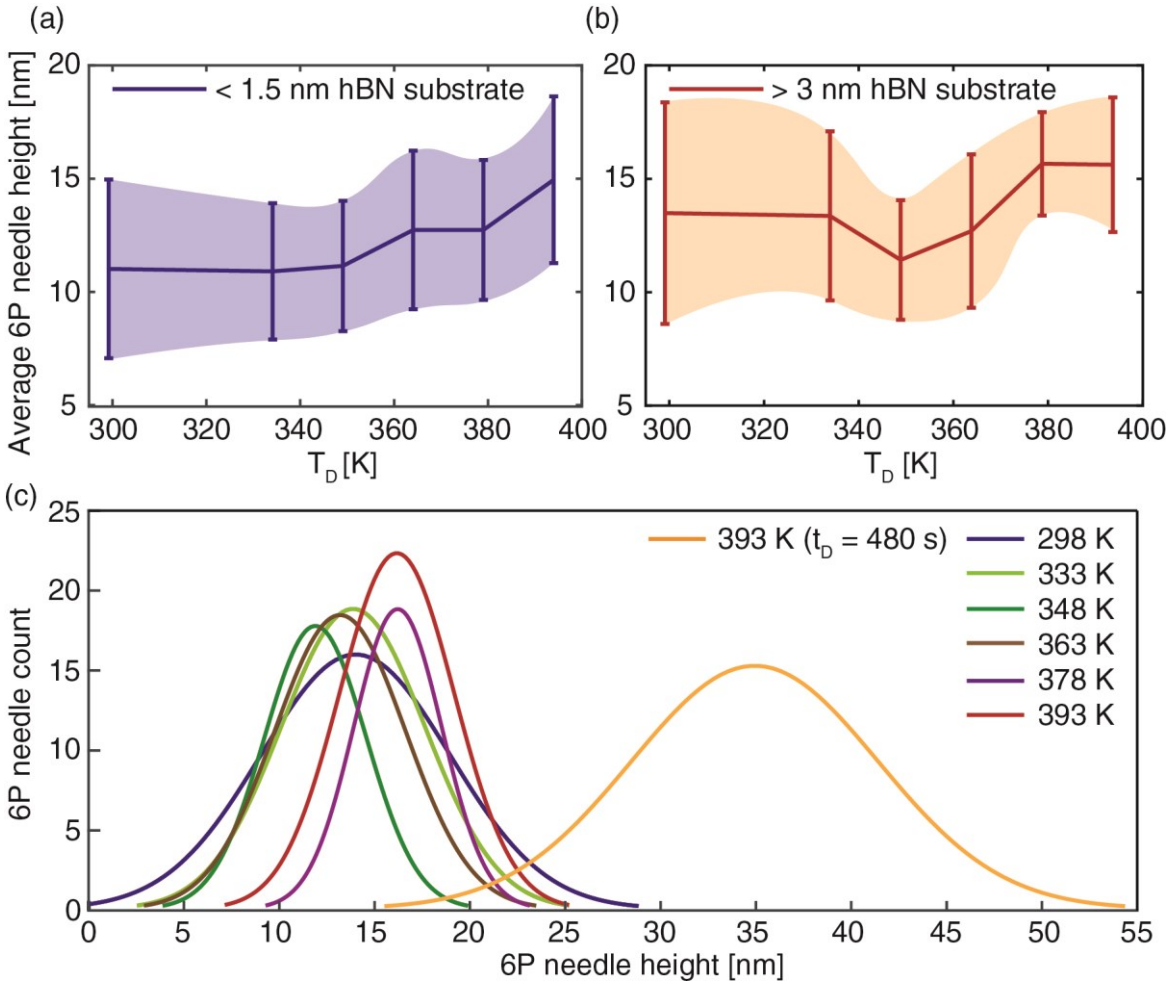

Figure 4.9: (a-b) Average 6P needle height as a function of T_D. The blue line in (a) shows the data for 6P needles grown on top of thin hBN flakes (below 1.5 nm thick) and the red line in (b) illustrates the data for 6P needles grown on bulk hBN flakes (above 3 nm thick). The shaded areas illustrate the standard deviations. (c) 6P needle height distribution for the bulk hBN flakes dependent on the T_D, including a sample at a T_D of 393 K with an increased t_D (orange line).

4.3.2. Effects on the resulting coverage of 6P

To study the dependence of the T_D on the resulting coverage of 6P on top of hBN the grain analysis tool, provided by the software package Gwyddion, was used [61]. The grains were marked by height threshold, and the volume related properties were calculated using three

different methods; zero basis, grain minimum basis, and Laplacian background basis. Zero basis calculates the volume between the needle surface and the plane that has been set to z = 0, which is the hBN substrate, often overestimating the volume. Grain minimum basis measures the volume between the maximum and the minimum value of the needles typically underestimating the volume. Laplacian background basis determines the volume between the needle surface and the basis surface formed by Laplacian interpolation of surrounding values. The latter is the most sophisticated method and was used to determine the mean values, while the other two were used to estimate the deviation, which was about ±20% of the mean value.

Figure 4.10 illustrates the application of the grain analysis tool, by the example of a 10 x 10 µm² AFM image of an hBN bulk flake at a T_D of 348 K. The needles were marked red via height threshold. Applying the obtained data it was possible to calculate the volume of the 6P molecules per unit area on hBN and SiO_2. As mentioned before, there is a significant difference between the three applied methods used to determine the needle volume and the marking of the needles proofed to be a bit problematic, especially at lower T_D. Nevertheless, this method should give a good estimation of the resulting 6P coverage.

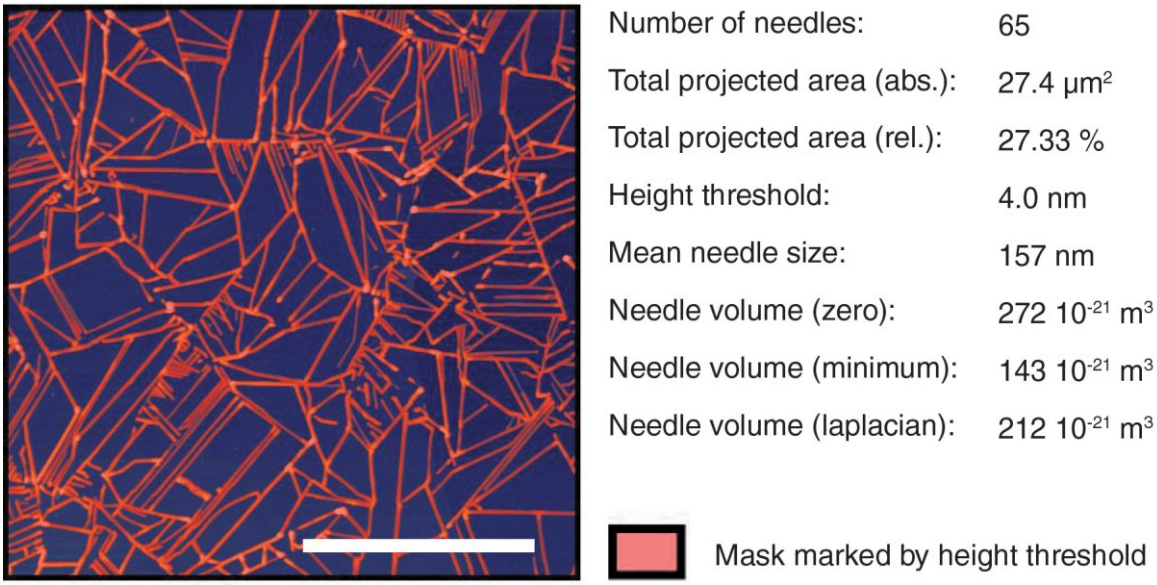

Figure 4.10: 10 x 10 µm² AFM topography images at a T_D of 348 K showing the application of the grain analysis tool and all received volume related properties on top of an hBN bulk flake. The red marked masked represents the area used to calculate the volume related properties (lateral scale bar 4 µm, z scale: 25 nm).

In order to get a better comparison, the 6P volume of thin hBN flakes (below 1.5 nm) and bulk hBN flakes was put into ratio with the 6P volume on SiO_2 at the same T_D. It is assumed that both 6P islands and 6P needles have the same molecular density, hence both crystallite types share the same herringbone structure as bulk. Therefore, the 6P volume per unit area on top of several hBN flakes and SiO_2 was obtained out of 10 x 10 µm² AFM topography images at

different T_D, using the method described above To rule out the influence of different local deposition rates on top of the samples, the coverage of 6P on SiO_2 was obtained close to the chosen hBN flakes.

The resulting ratio of 6P volume on hBN/SiO_2 is presented in Figure 4.11. It can be seen that the volume ratio is reduced as the T_D is increased. However, there seem to be slight differences between thin and bulk hBN flakes. These minor deviations can most likely be explained due to the fact that 6P volume was harder to receive on top of the thin hBN flakes since they were much smaller than bulk hBN flakes. Therefore, the required 10 x 10 µm² image size could not always be obtained. Although the volume ratio is greater than one, it does not necessarily mean that the sticking probability of 6P is higher on hBN than on SiO_2. It also has to be taken into account that the 6P growth mechanisms on these two substrates differ significantly. While the 6P needles can grow to a height of up to 30 nm, the islands are just around 2.5 nm tall, only forming additional layers at higher T_D. Therefore, the amount of 6P molecules contained inside of the needles is about an order of a magnitude higher than the islands covering the same area. Furthermore, hence the 6P needles leave more of the surface area bare than the islands, the uncovered hBN provides a higher sticking probability than the already covered SiO_2. As a result, the 6P uptake on hBN is increased. Similar behaviour was also reported for the epitaxial growth of 6P on graphene/SiO_2 [44].

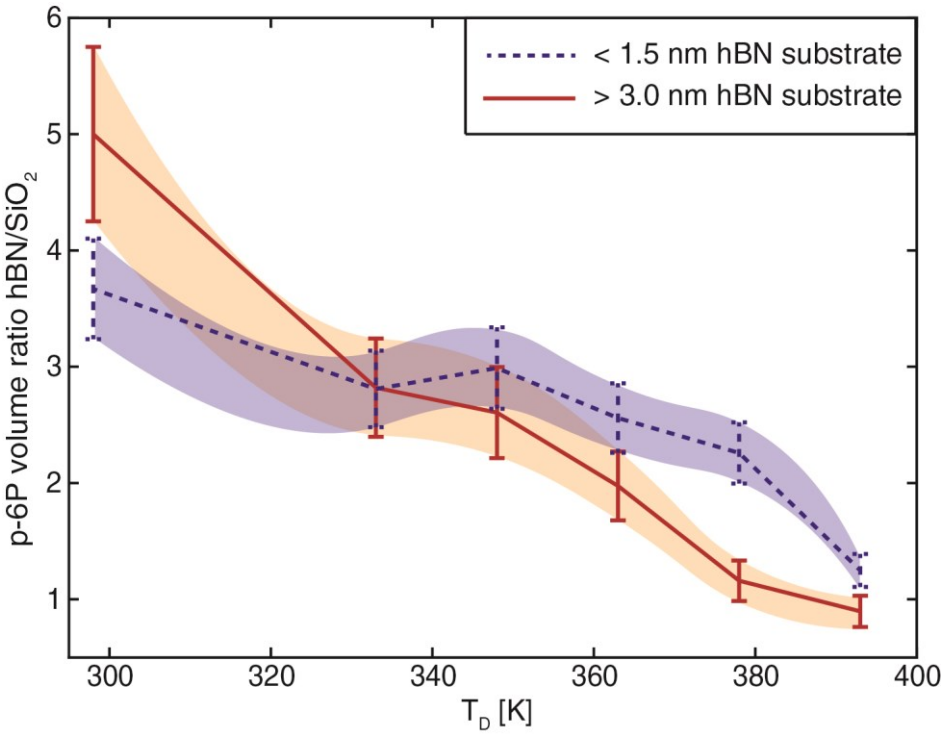

Figure 4.11: 6P volume ratio hBN/SiO_2 as a function of T_D. The solid red line represents the data for 6P volume ratio on top of bulk hBN flakes and the blue dashed line the data for 6P volume grown on thin hBN flakes (< 1.5 nm). The shaded areas illustrate the deviations.

To better understand the resulting 6P volume ratio of hBN/SiO_2, it was necessary to take a closer look at the deposited 6P volume per unit area on hBN and SiO_2 respectively. Figure 4.12 illustrates the dependence of the 6P volume on the T_D. The 6P volume on top of bulk hBN flakes behaves almost identically to the one on thin hBN flakes and thus was not displayed to make the graph more coherent. Lower coverage of 6P at higher T_D was reported for other vdW substrates, as graphene and mica [44,69]. This can be associated with desorption of molecules from the surface at higher T_D. However, for this case, the measured 6P coverage on top of SiO_2 constantly increases with raising T_D, while on hBN it shows a more rapid increase up to a peak at a T_D of around 363 K, followed by a decrease of 6P coverage. There are several impact factors that might lead to the observed phenomenon of decreasing sticking probability of 6P on top of hBN and SiO_2 at lower T_D. First of all, although the 6P molecule deposition was performed using the same growth parameters, the deposition rate could not be observed in-situ, therefore, a constant deposition rate cannot be guaranteed. Furthermore, a reduced diffusion radius of 6P molecules at low T_D could lead to desorption of the molecules before they can attach to already existing island or needle borders or form stable nuclei. However, previous growth experiments with 6P revealed almost complete condensation up to about 400 K [69]. The most likely explanation is that the used method slightly underestimates the 6P volume at the island and needle borders. Since at lower T_D there are more small islands and short needles, this effect would lead to the observed reduced sticking probability at low T_D. Nevertheless, taking all these factors into account it can be concluded that on top of hBN at a T_D of about 360 K the sticking probability starts to decrease.

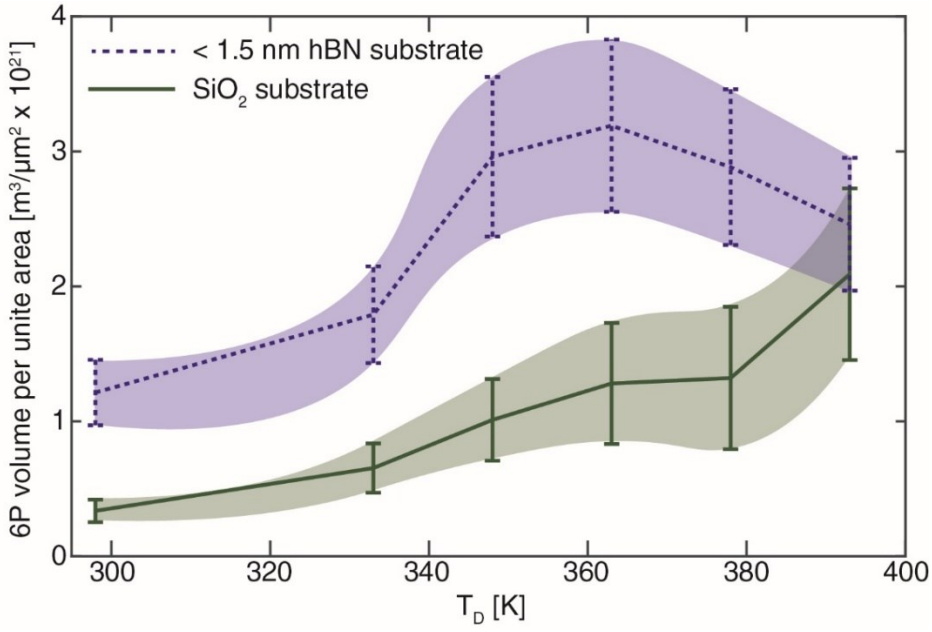

Figure 4.12: 6P volume per unit area depending on the T_D. The blue dashed line shows the data for 6P volume grown on hBN flakes with a thickness below 1.5 nm while the solid green line represents the volume on SiO_2. The shaded areas illustrate the deviations.

4.4. Influence of the hBN substrate thickness

As found previously, the thickness of the hBN support has a clear impact on the morphology of the resulting 6P crystallites. To further investigate this issue, hBN flakes of varying thickness deposited at a fixed T_D of 363 K were analysed according to their 6P needle length and orientation. T_D = 363 K was chosen due to exhibiting high coverage, while also not having too long 6P needles enabling statistical analysis at a reasonable AFM image size. Furthermore, the sample prepared at this T_D had the largest amount of hBN flakes with a vast variety in thickness.

4.4.1. Effects on the morphology of 6P

To investigate the influence of the hBN thickness on the length of the resulting 6P needles, several hBN flakes reaching from a thickness of below 1 nm to above 20 nm were analysed, using the same method described in the previous chapter.

The resulting graph is presented in Figure 4.13. Each data point represents an hBN flake with a certain number of layers, while the shaded areas illustrate the standard deviations. More than 100 needles on each flake were taken into account, out of 10 x 10 µm² AFM topographical images.

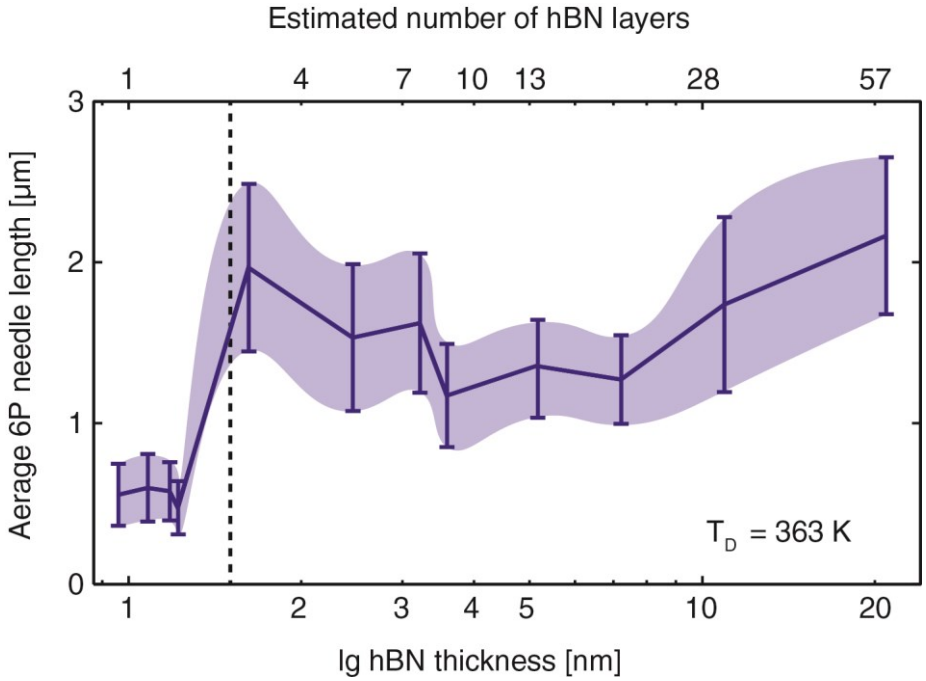

Figure 4.13: The dependence of 6P needle length on the thickness of the hBN substrate. Each data point connected with a solid blue line represents an hBN flake. The shaded areas illustrate the standard deviations, while the dotted black line represents a flake thickness of 1.5 nm.

There is a significant difference between hBN flakes thinner than 1.5 nm compared to the ones with more hBN layers. While thinner hBN flakes show an average needle length of about 0.6 µm, thicker hBN flakes have over 3 times longer needles in average. The length of 6P needles was not found to increase any further as soon as the hBN substrate reached a thickness of about 1.5 nm. Even flakes well over 20 nm showed a similar growth behaviour like the ones at a height slightly above 1.5 nm.

To determine the orientation of the 6P needles, again the distance tool provided by the software package Gwyddion was used. For this analysis, the main variable was the azimuth φ, providing the angle between the measured 6P needle and the baseline of the AFM image [61]. Furthermore, to create a convincing histogram of the 6P needle orientation not only the number but also the length of the needles of a certain orientation was considered. Therefore, also the total planar distance (R) of each 6P needle was taken into account. Using the multi-paradigm numerical computing environment MATLAB, a program was created to sum up the total needle length of a chosen orientation range plotted into a histogram.

Three hBN flakes with a thickness of about 1 nm, 1.6 nm, and 21 nm were chosen for further analysis of the 6P needle growth direction. To rule out measurements errors of the angular distribution, the 6P needles were displayed with a ± 2.5° tolerance, and on every flake the 100 longest needles were taken into account. During the mechanical exfoliation process, the hBN flakes are most likely to break along an armchair or zigzag orientations. Therefore, it can be assumed that long straight hBN flake edges follow one of those two directions. Furthermore, due to the geometry of the 6P molecule and its behaviour on similar vdW materials such as graphene [12,16,43-44], it is suspected that the 6P needle growth direction should be correlated to the armchair and zigzag orientations of the hBN substrate. The investigated hBN flakes and their respective 6P needle orientation are displayed in Figure 4.14. The sample supported by the thin hBN flake below 1.5 nm did not only have much shorter 6P needles than the samples supported by thicker hBN substrate but also did not show a clearly resolved angular distribution of the 6P needles. On the contrary, the samples with an hBN flake thickness of about 1.6 nm and 21 nm followed a tri-fold rotational symmetry of the underlying hBN substrate. Therefore, it can be concluded that the majority of the 6P needles are either growing in armchair or zigzag direction, which will be discussed in detail in the following chapter of this thesis. Furthermore, upon reaching an hBN thickness of above 1.5 nm, a further increase of thickness did not prove to influence the 6P needle morphology or their orientation, indicating that all investigated hBN thickness related effects are terminated at a thickness of above 1.5 nm (3-4 hBN layers).

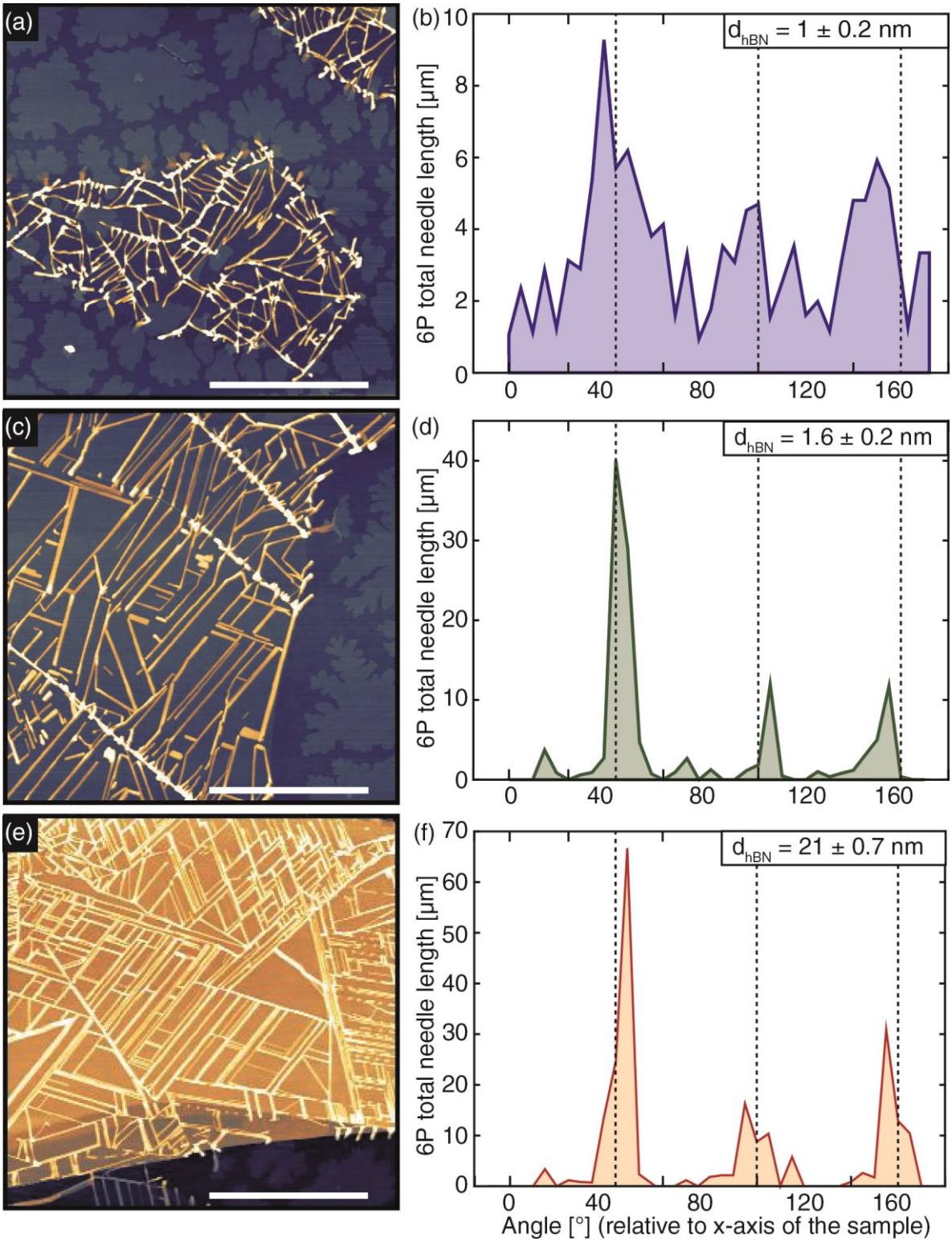

Figure 4.14: 10 x 10 µm² AFM topographical images of the further analysed hBN flakes of different thickness (a, c, and e) with their adjacent 6P needle growth direction (lateral scale bars 4 µm, z scales: 20 nm (a), 25 nm (c), 45 nm (e). hBN flake thickness (d_{hBN}): 1 ± 0.2 nm (a), 1.6 ± 0.2 nm (c), 21 ± 0.7 nm (e)). The x-axis displays the 6P needle growth direction [deg] while the y-axis shows the total length of 6P needles [µm] (b, d, and f). The dashed black lines correspond to the hBN flake edge orientation.

4.4.2. Contributing factors to the hBN thickness effects

In order to understand the experimentally observed influences of the hBN thickness on the 6P needle growth, several direct and indirect contributing factors have to be taken into account.

To analyse whether the observed effect is a direct influence of the hBN thickness, density function theory (DFT) calculations of 6P on one and three layers of hBN were performed respectively. All DFT calculations were done by the group of Assoc.-Prof. Dr. Peter Puschnig from Karl-Franzens-Universität Graz, Austria. The density functional theory is a framework to specify the quantum mechanical ground state of many-electron systems, using the spatially dependent electron density. It is used to calculate fundamental properties of molecules and condensed phases, such as bond length and bond energy. Due to experiences with 6P on other similar vdW substrates the two most likely alignments of the 6P molecule were considered. One with the long axis oriented along the zigzag direction and one along the armchair direction of the hBN substrate. The most stable adsorption sites were calculated for each orientation and the respective adsorption energies were determined, respectively. Figure 4.15 illustrates an example of the model with three hBN layers used for the DFT calculations, with the 6P molecule lying alongside the armchair configuration on top of the hBN substrate.

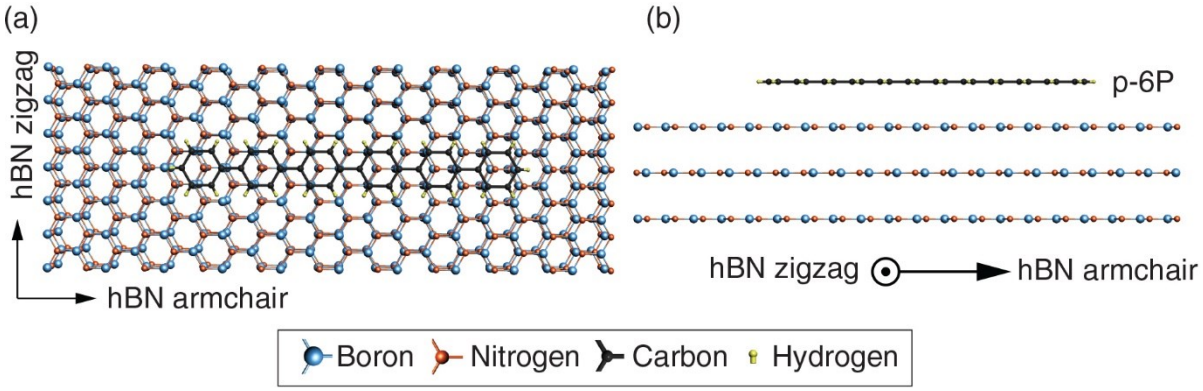

Figure 4.15: Modell used to calculate the most stable adsorption sites and respective adsorption energies for a single 6P molecule on top of a three-layer hBN substrate, viewed from the top (a) and from the side (b). The arrows indicate the zigzag or armchair direction of the hBN substrate. DFT calculations performed by Dr. D. Lüftner and Prof. P. Puschnig, Graz University.

The calculated adsorption energies did not show any dependence on the change of the hBN substrate thickness. Therefore, it can be assumed that another indirect mechanism must cause the experimentally observed layer dependent changes in growth behaviour of 6P crystallites.

To explain the change of the 6P morphology a closer look was taken into two contributing factors that arise from the hBN/SiO_2 interface.

First of all, although, SiO_2 has an extremely flat surface already, hBN, being a vdW substrate should have one a magnitude smoother than that [45]. The question remains if an hBN flake is influenced by the underlying SiO_2 substrate and if yes at what substrate thicknesses this effect is terminated. Higher surface roughness has been observed to influence the growth and performance of other organic semiconductors as pentacene [25] and is expected to also influence the growth of 6P.

Therefore, the roughness of several hBN flakes of varying thickness was measured and compared to the roughness of the surrounding SiO_2 surface. To determine the roughness of the hBN flakes the statistical analysis tool provided by Gwyddion was used. It calculates the root mean squared (RMS) roughness of the measured height deviations taken within the evaluation length and measured from the mean line out of a recorded AFM image. Where R_q is the RMS roughness, n the evaluation length and r the profile height [61]

$$R_q = \sqrt{\frac{1}{n}\sum_{j=1}^{n} r_j^2} \qquad 4.2$$

Figure 4.16 illustrates the resulting hBN surface RMS roughness in dependence of the hBN flake thickness and RMS roughness of their surrounding SiO_2 surface. The data was obtained from an average of ten 1 x 1 µm² AFM images for every hBN flake surface of varying thickness and surrounding SiO_2 surface. The roughness analysis revealed that the surface of the hBN flakes below 1.5 nm had an average roughness of 0.24 nm, which is comparable to the measured roughness of the surrounding SiO_2 surface of 0.23 nm. In comparison, the roughness of the hBN flakes thicker than 1.5 nm was found to be much smoother with an average value of 0.16 nm. However, since the measured surfaces are incredibly smooth, with a measured RMS roughness in the Angstrom regime, it cannot be ruled out that some of that roughness is created through external influences on the AFM measurements. Therefore, it is ambitious to claim absolute values for the hBN surface RMS roughness with the AFM under ambient conditions. Nevertheless, should there be unanticipated influences on the roughness measurements, they would affect the measurements on thin and bulk hBN flakes alike. Consequently, considering that the roughness of thin hBN flakes was found repeatedly to be rougher than on bulk and FL hBN flakes, it can be assumed that they are influenced by the underlying SiO_2 substrate.

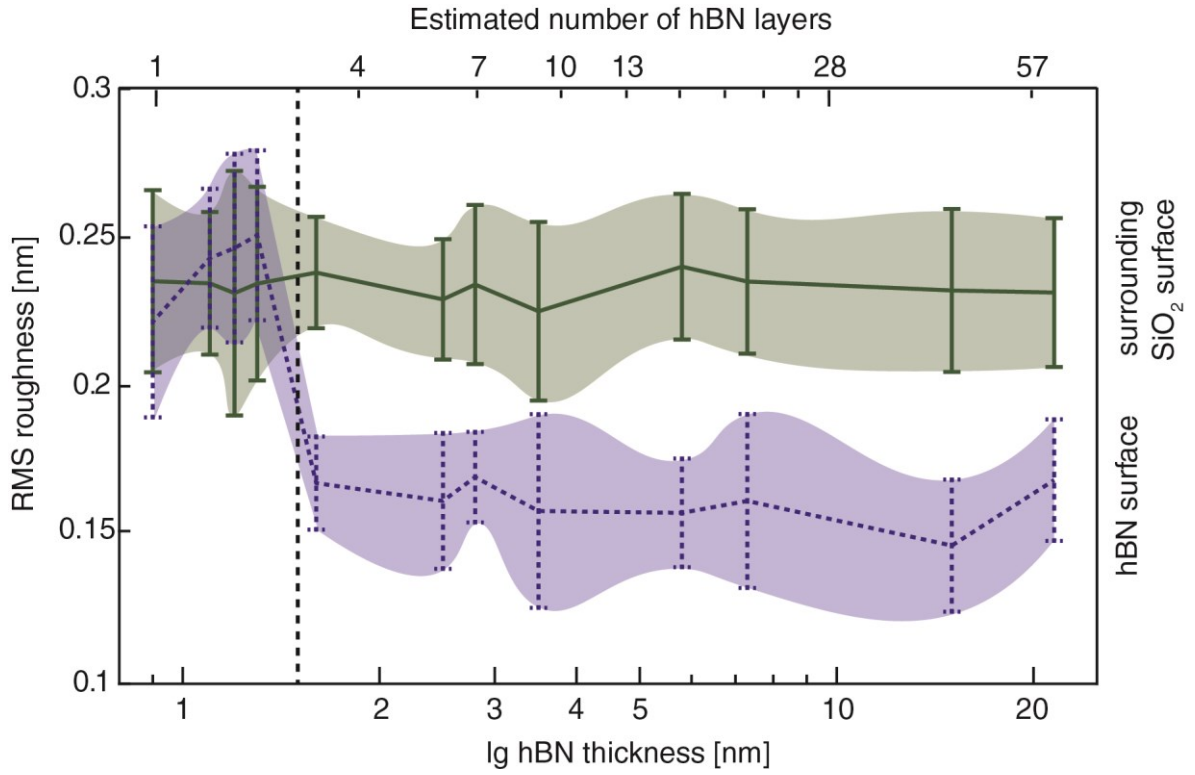

Figure 4.16: Analysis of the RMS roughness of the hBN surface in dependence of the hBN flake thickness (dotted blue line) and the RMS roughness of their surrounding SiO_2 surface (solid green line). The shaded areas illustrate the standard deviations, while the dotted black line represents a flake thickness of 1.5 nm.

There has been found no significant roughness difference between hBN flakes with a thickness between 1.6 nm and 20 nm, indicating that the influences of the underlying SiO_2 substrate should be terminated after a few hBN layers. However, this can only be said for hBN flakes on top of smooth substrates such as SiO_2. The roughness influence from a rougher substrate is expected to be increased and it might take several more layers to eliminate the effect.

Another influence could be due to a trapped water layer beneath the hBN flake and the SiO_2 substrate, introduced during the mechanical exfoliation, giving rise to a dipole field. It has been shown that similar to other vdW substrates such as graphene or MoS_2 [71-72], the decay of the dipole field of hBN follows the 3D nonlinear Thomas-Fermi theory, as illustrated in Figure 4.17. Since hBN is an insulator, the addition of hBN layers is not very effective in screening of the dipole field and it decays much slower with addition of hBN layers compared to graphene or MoS_2, just being able to completely shield the introduced dipole field at an hBN substrate thickness of about 100 nm (300 hBN layers). Therefore, this mechanism should not be responsible for the observed change of growth behaviour of 6P crystallites on mono-layer hBN flakes compared to bulk hBN flakes. However, compared to subsequent hBN layers, it

was reported that the first hBN layer has a much weaker screening, which is possibly induced due to more charge transfer between the underlying water film and the first hBN layer [73].

The presence of a dipole field, induced by an underlying water layer, was already studied before for pentacene grown on graphene [71]. Although the screening of the graphene layers is more than an order of magnitude stronger compared to hBN, the underlying water layer was found to have a significant impact on the growth behaviour of pentacene. While a water layer was present, it grew as islands whereas needles formed when the layer was suppressed. Therefore, we can claim that the presence of an underlying water layer beneath the hBN substrate also should have an influence on the growth of 6P crystallites.

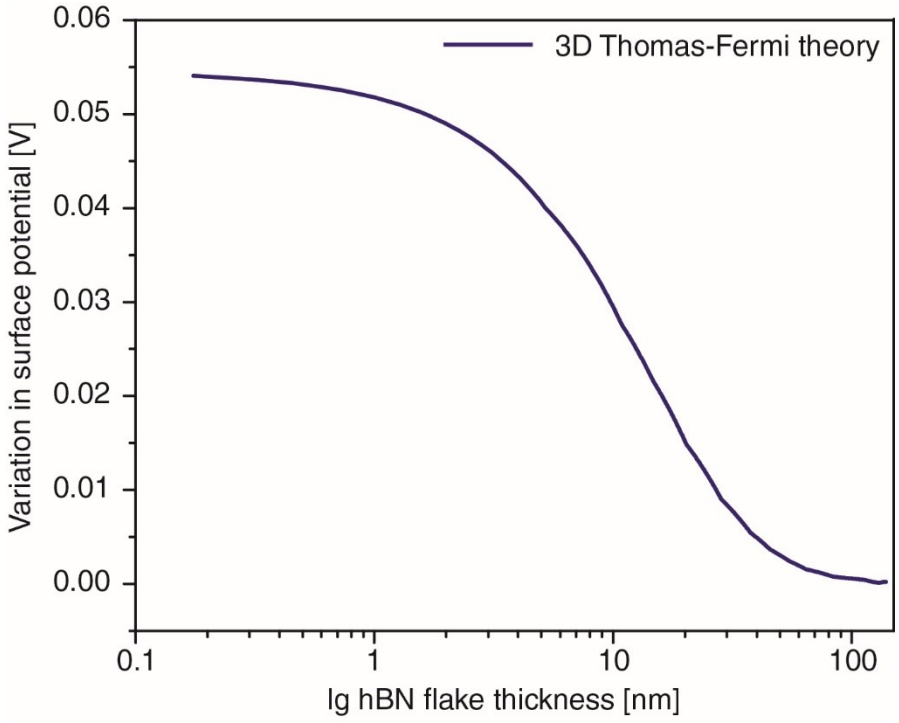

Figure 4.17: Deviations in the surface potential caused by unscreened charges for different hBN thicknesses, according to the 3D nonlinear Thomas-Fermi theory taken from reference 73.

It is reasonable that both, the increased roughness as well as the weaker shielded dipole field, influences the growth behaviour of the 6P crystallites on hBN flakes below a thickness of 1.5 nm. Therefore, in order to obtain well organised and long 6P needles on hBN flakes with a SiO_2 substrate it is necessary to reach a critical hBN support thickness of above 1.5 nm.

4.5. Epitaxial relation of 6P and hBN

As soon as the hBN flakes reached a critical thickness of above 1.5 nm, 6P was found to form highly ordered networks of needle-like crystallites, following high symmetry directions of the hBN flakes. Therefore, the focus is now shifted from mono- or bi-layer hBN flakes to bulk hBN flakes for further analysis. In order to determine the exact adsorption position of 6P on the hBN substrate, the needle orientation on top of several hBN bulk flakes in a T_D range from 298-393 K was analysed.

4.5.1. Angular distribution of 6P needles on hBN

To determine the angular distribution on top of the hBN substrate the same method as in chapter 4.4.1 was used. Although the measuring of the needles was done manually it proved to be highly accurate, only showing slight difficulties concerning very short needles. Therefore, the tolerance for the histogram was now narrowed down to ±0.5°.

Figure 4.18 and 4.19 illustrate the angular distribution of the 6P needles on top of the hBN substrate with their respective topological AFM images. On top of every hBN flake, the 100 longest needles were measured for analysis. At lower T_D (298-348 K), the data was taken from 10 x 10 µm² AFM images (Figure 4.18 (a), (c) and (e)). For higher T_D (363-393 K), the data had to be obtained from 20 x 20 µm² (Figure 4.19 (a) and (c)) and 30 x 30 µm² AFM images (Figure 4.19 (e)), due to the increasing length of the 6P needles. The solid lines resemble the directions of the sharp flake edges and they were separated by an integer multiplier of 30°, corresponding to the zigzag and armchair direction of the hBN flakes. It has to be noted that, although hBN flakes are more likely to break along those orientations, it is no necessity and only perfectly straight edges can be taken into account. However, also rather straight edges deviating from armchair or zigzag direction of the hBN flakes have been observed, allowing the use of this method only as an aiding tool.

As already shown before, the large majority of 6P needles tends to follow only one of the orientations forming three peaks separated by 60° seen in Figure 4.18 (b), (d), (f) and 4.19 (b), (d), (f). Interestingly, the reduced tolerance of ±0.5° for orientation range revealed that the amount of 6P needles growing exactly in the direction of the main orientation was almost zero. Instead, there is a clear split of about ±5° to the main orientations, separating into six peaks, indicated by the green dotted lines. This effect is not clearly visible at a T_D of 298 K perhaps due to the short needle length, increasing the error of the orientation measurements.

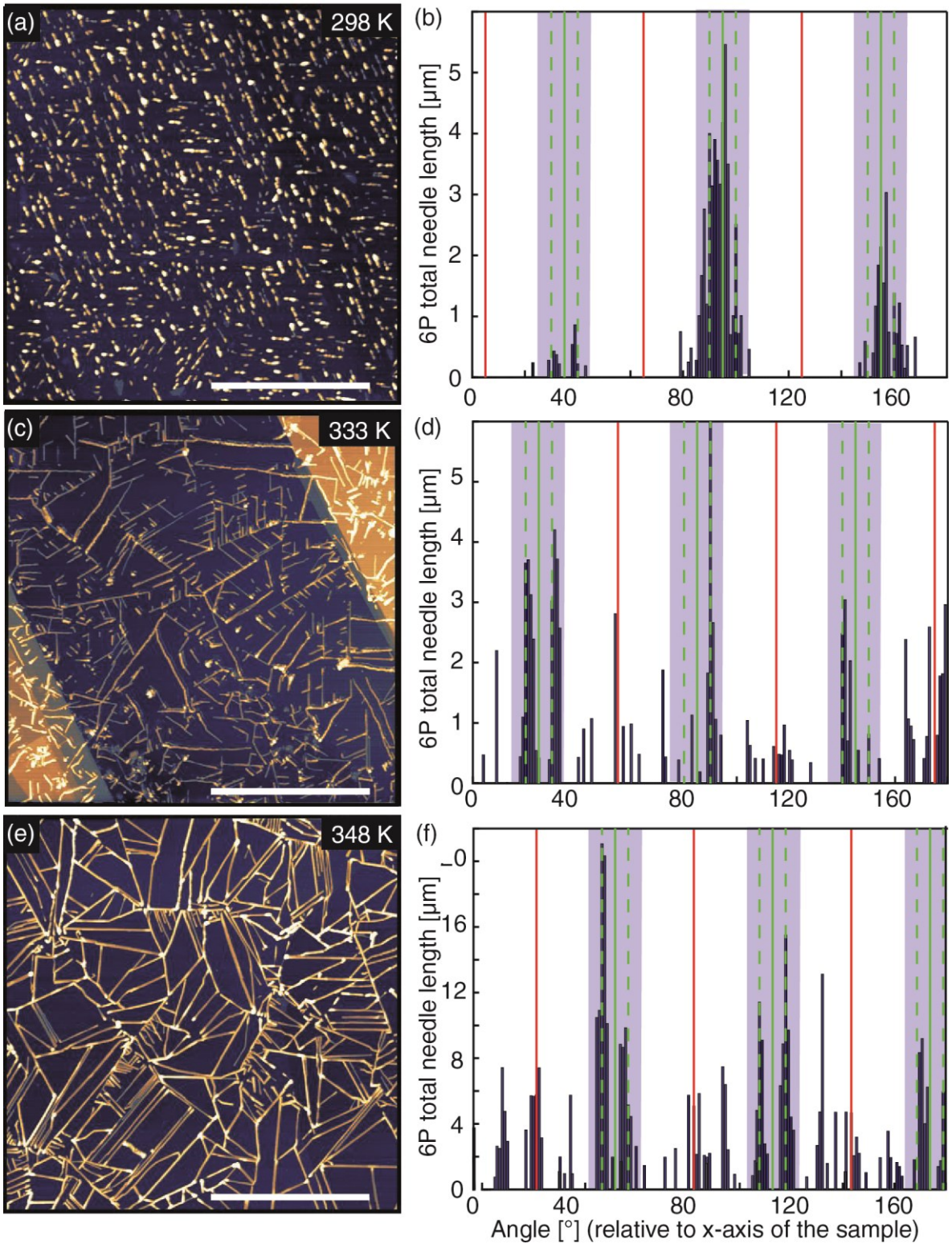

Figure 4.18: 10 x 10 µm² AFM images at different T_D (a, c, and e) with their adjacent 6P needle growth directions (lateral scale bars 4 µm, z scales: 30 nm (a), 25 nm (c), 15 nm (e)). The x-axis displays the 6P needle growth direction with ±0.5° accuracy, while the y-axis shows the total length of 6P needles in the corresponding direction (b, d, and f). The solid green and red lines resemble the hBN flake edge orientations. The green dotted line represents ±5° and the blue shaded areas ±10° deviations from the observed main growth orientations.

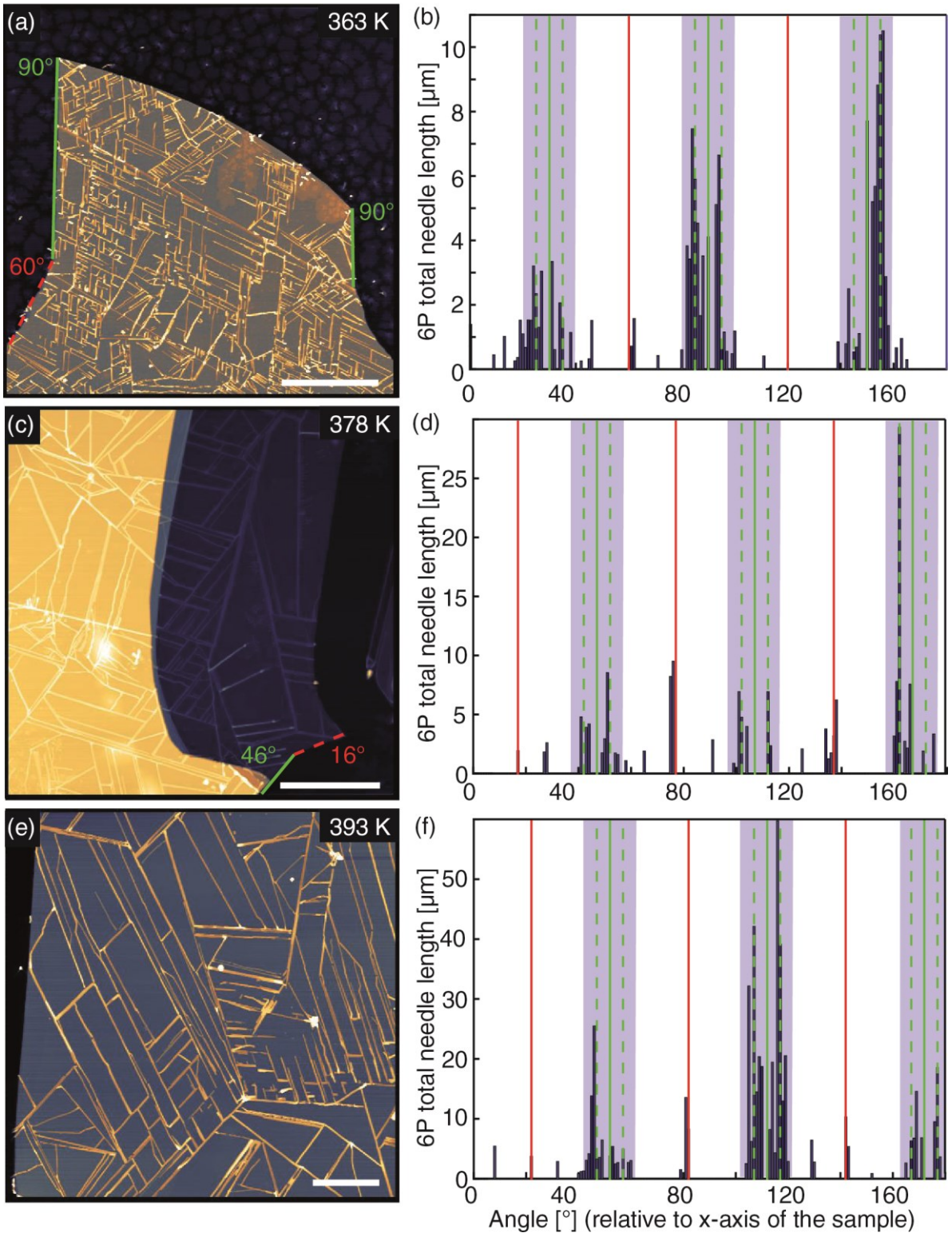

Figure 4.19: 20 x 20 µm² (a, c) and 30 x 30 µm² (e) AFM topographical images at different T_D with their adjacent 6P needle growth directions (lateral scale bars 5 µm, z scales: 45 nm (a), 130 nm (c), 60 nm (e)). The x-axis displays the 6P needle growth direction with ±0.5° accuracy, while the y-axis shows the total length of 6P needles (b, d, and f). The solid green and red lines resemble the hBN flake edge orientations. The green dotted line represents ±5° and the blue shaded areas ±10° deviations from the main growth orientations.

With increasing T_D the total 6P needle length growing in preferred ±5° split orientations seemed to increase. Therefore, the total length of 6P needles of the blue shaded areas in Figure 4.18 and 4.19 ±10° of the main orientation have been summed and divided by the total 6P needle length on the flakes. The resulting diagram can be seen in Figure 4.20. The blue shaded area represents the amount of 6P needles growing in the selected orientation range. With increasing T_D the amount of needles growing in main orientations overall increases. Since one-third of all possible growth directions were considered as preferred, the dotted red line represents the case for a completely disordered 6P needle network. Since the total 6P needle length in the selected orientation range clearly surpasses the case of a completely disordered 6P needle network at every T_D, it is indicated that these directions are energetically preferred.

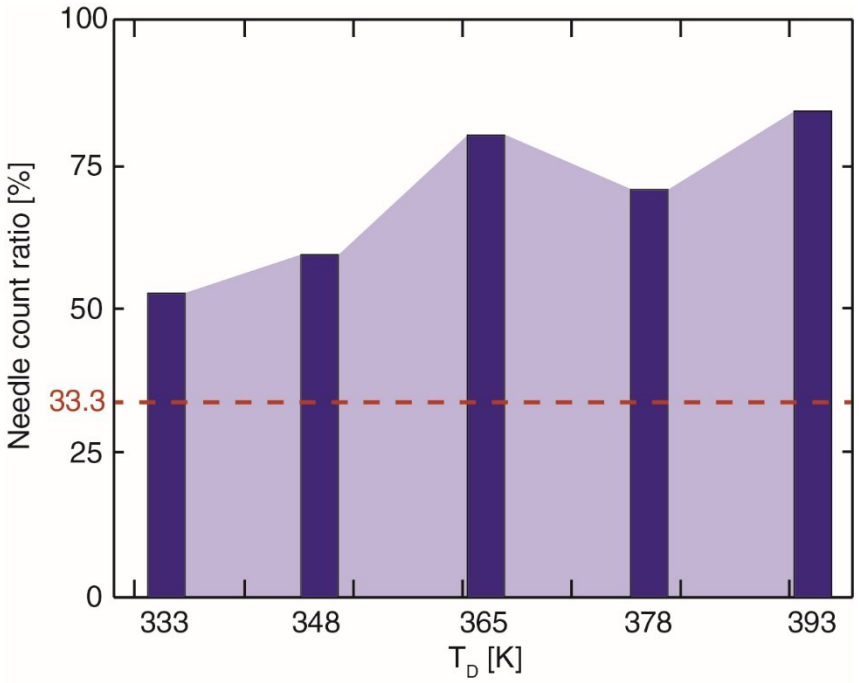

Figure 4.20: Ratio of 6P needles growing in preferred growth direction as a function of T_D. The red dotted line represents the amount of needles for a completely disordered 6P needle network.

In Figure 4.20 no data point was presented at a T_D of 298 K since almost no 6P needles following the main growth orientations were observed. Hence only the 100 longest needles were taken into account the first question was if at this T_D the needles not growing in preferred orientation are just too small to assign them a direction. However, the analysis of the average 6P needle length at higher T_D revealed, that the average length is independent of the growth direction. Another explanation would be that at low T_D (≤ 298 K) the 6P molecules do not have enough energy to grow outside of the energetically most favourable directions. Above a T_D of 333 K, they can also grow along non-energetically preferred directions. However, with rising T_D the diffusion radius of 6P molecules increases, enabling them to move to energetically more

favourable positions, explaining the decrease of 6P needles not growing in preferred orientations. The increased mobility and diffusion radius of the 6P molecules at higher T_D also explain the observed large bare areas on top of the hBN flake (Figure 4.19 (e)) compared to the dense 6P needle population at lower T_D (Figure 4.18 (a)).

To quantify these assumptions, the number of 6P needles dependent on the T_D has been analysed. The data was received as a combination of counting the 6P needles manually and calculations using already previously determined parameters, as average 6P needle length, and deposited 6P volume. The resulting graph is presented in Figure 4.21, indeed revealing a decrease of the needle density with increasing T_D.

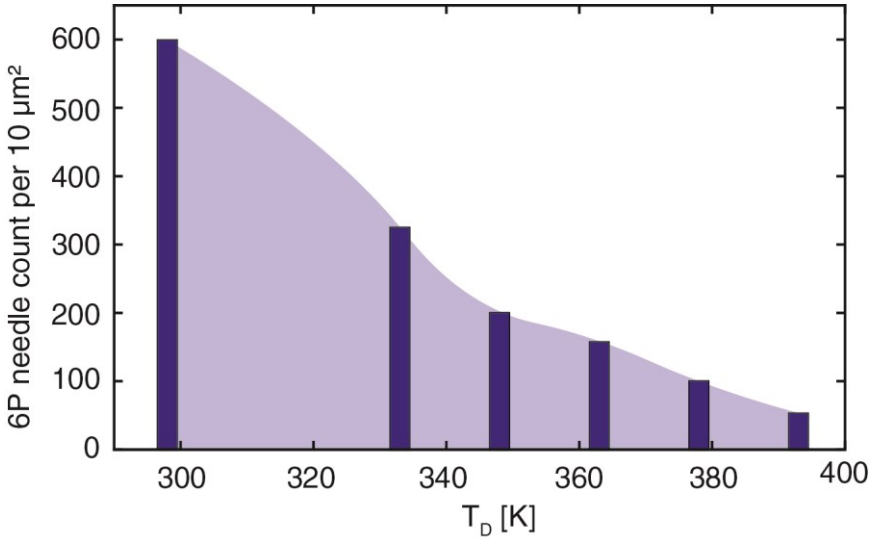

Figure 4.21: 6P needle count per 10 µm² on top of hBN as a function of T_D.

4.5.2. Adsorption position of 6P on hBN

With the help of the AFM measurements analysis and the angular distribution of the 6P needles on hBN, it was possible to narrow down the preferred growth direction to either follow the armchair or the zigzag orientation of the hBN substrate. Previous experiences with the growth of 6P on graphene [44] indicate an adsorption of the molecule with the long axis parallel to the armchair direction of the hBN substrate. Furthermore, pentacene has shown to align along the zigzag direction on top of hBN [10]. Therefore, to determine the exact adsorption position of 6P on top of hBN first-principle calculations within the framework of DFT have been performed by the collaboration partners of Graz University, as previously described in chapter 4.4.2.

The adsorption energies of a single 6P molecule on top of a mono-layer hBN substrate were calculated for four adsorption sites with 6P oriented along the zigzag direction (Figure 4.22) and nine different adsorption sites with the long axis orientated along the armchair direction (Figure 4.23) of hBN. For the armchair direction, every consecutive ring aligns in the same

position in relation to the hBN substrate, whereas, following the zigzag direction only the fourth consecutive ring ends up in an equivalent position. The adsorption energies for the illustrated 6P adsorption positions are listed in Table 4.1.

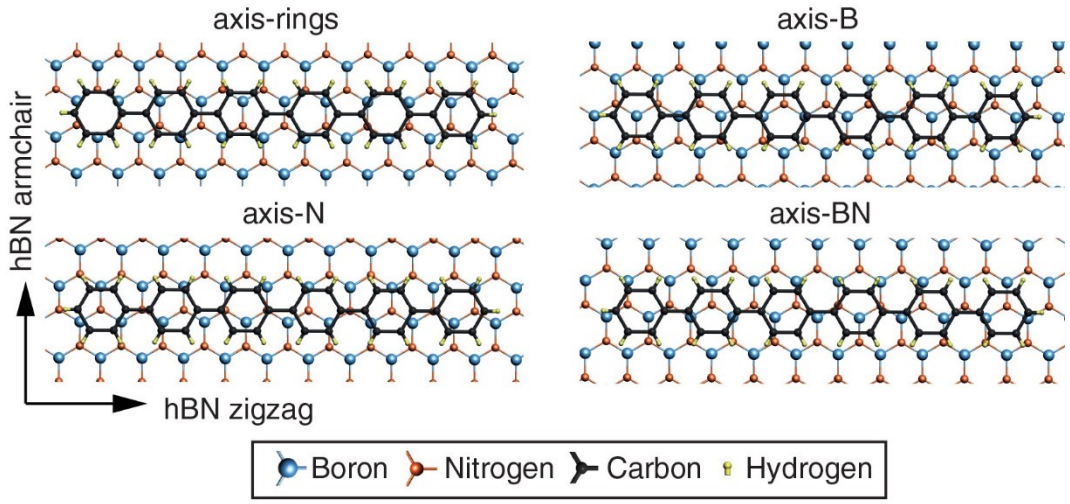

Figure 4.22: Adsorption sites of the 6P molecule oriented along the zigzag direction of the hBN substrate used to calculate its respective adsorption energy.

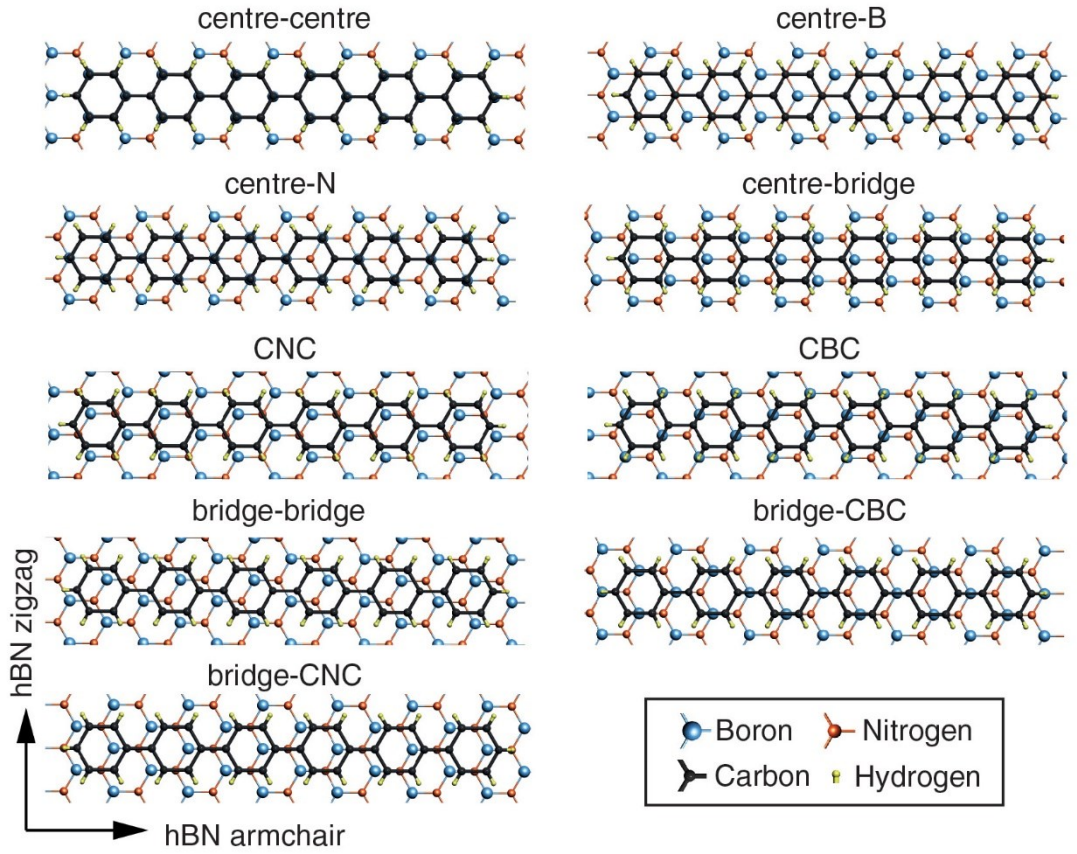

Figure 4.23: Adsorption sites of the 6P molecule orientated along the armchair direction of the hBN substrate used to calculate its respective adsorption energy.

Table 4.1: Adsorption energies calculated within the framework of DFT of the in Figure 4.22 and 4.23 illustrated adsorption sites of a single 6P molecule orientated along the zigzag and the armchair direction of the hBN substrate. Performed by Dr. D. Lüftner and Prof. P. Puschnig, Graz University.

Adsorption site	axis-rings	axis-B	axis-N	axis-BN
E_{ads} [eV]	-3.3618	-3.3580	-3.3597	-3.3701

Adsorption site	centre-centre	centre-B	centre-N	centre-bridge
E_{ads} [eV]	-3.2486	-3.3457	-3.5410	-3.3899

Adsorption site	CNC	CBC	bridge-bridge	bridge-CBC	bridge-CNC
E_{ads} [eV]	-3.3581	-3.4213	-3.3339	-3.3662	-3.4680

In all cases, it was found that the average distance between 6P and the hBN substrate is about 3.3 Å . The energetically most favoured adsorption site is with the centre of the phenyl rings above the nitrogen atom of the hBN substrate with the 6P molecule axis orientated parallel to the armchair direction (-3.5410 eV). The adsorption energy for this position is about 70 meV smaller than the next stable one along an armchair direction (-3.4680 eV) and 170 meV more favourable than the most stable position with the 6P molecule orientated in a zigzag direction (-3.3701 eV).

Taking into account that during the initial growth stages single 6P molecules adsorb along the armchair directions of the hBN substrate and further deposited molecules will attach vertically to the long axis of the molecule, the preferred growth direction of the 6P needles is along the zigzag direction of the hBN substrate. In this way, it also is possible to identify the highly-symmetric orientations of the hBN substrate, without atomic resolution or the use of special characterisation techniques. However, this cannot explain the observed ±5° rotation of the 6P needles along the hBN substrate zigzag direction. In order to check if the small variation of the growth direction can be explained by a slight rotation of the individual 6P molecules the adsorption energies with a rotation angle up to 8° from the most energetically favoured position were determined via DFT calculations.

Figure 4.24 illustrates the relative change of the adsorption energy of the 6P molecule corresponding to slight changes in rotation from the preferred growth direction, while the dotted blue line resembles the observed ±5° rotation of 6P on top of hBN. The 6P molecule is able to rotate ±2° from the preferred adsorption orientation without an increase of adsorption energy,

however with further rotation the energy increases. At a rotation angle of ±5° from the preferred adsorption site, the adsorption energy is about 75 meV higher even surpassing other positions along the armchair orientation. Therefore, this assumption can be ruled out as a reason for the deviation of the 6P needles from the high symmetry directions of the hBN substrate.

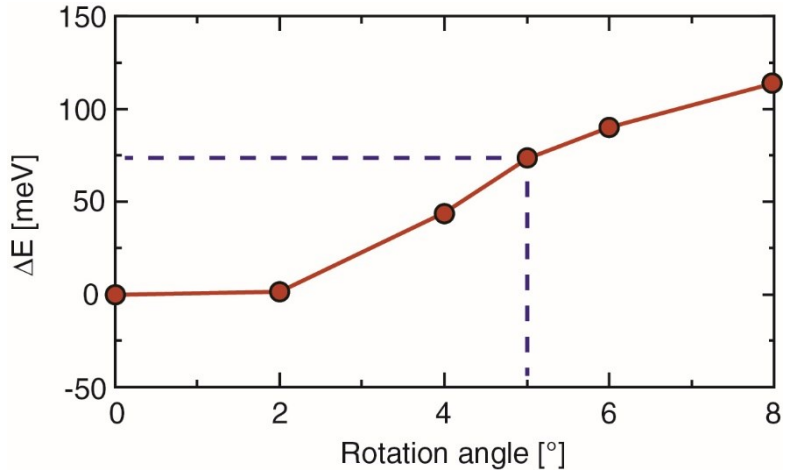

Figure 4.24: Relative change of the adsorption energy of the 6P molecule with rotation from the preferred adsorption site. The dotted blue line represents the observed ±5° rotation from the armchair direction of the long axis of the 6P molecule on top of the hBN substrate. DFT calculations performed by Dr. D. Lüftner and Prof. P. Puschnig, Graz University.

4.5.3. Contact plane of 6P needles on hBN

Since the rotation of the individual 6P molecules alone is not able to explain the observed ±5° rotation of the 6P molecules from the preferred growth direction along zigzag orientation, an alternative explanation has to be found. Therefore, the epitaxial relation between the 6P crystallites and the hBN substrate has been analysed by Dr. A. Matković in our group.

While for the initial stages of the 6P growth, the substrate-molecule interaction dominates and the molecules favour to occupy their individual equilibrium positions, this does not have to be the case with increasing molecule coverage. At a critical molecule density, the substrate-molecule interactions are taken over by intermolecular interactions of the 6P molecule, and they reorganise into an equilibrium bulk structure. Since at that point, the 6P crystallites are large enough to be considered bulk structures, the only possible structure at the chosen T_D is the monoclinic ß-phase, also called Baker structure of 6P crystallites [39]. However, also the interaction of the 6P molecules with the substrate has to be considered. The energetically most favoured contact plane would be the one introducing the least amount of strain between the equilibrium adsorption sites of individual molecules and the crystallite bulk structure.

In literature 6P crystallites were found to form several different contact planes on various single crystal substrates as mica (001) [66], KCl (100) [67] and Cu (110) [62,74]. Thereby, different contact planes lead to slight changes of the direction of the long needle axis (LNA) and substrate surface unit cell as listed in Table 4.2. Structure (a) represents the standard ß-phase structure. The resulting 6P molecule alignment for the respective contact planes is illustrated in Figure 4.25.

Table 4.2: Crystal contact planes reported for 6P, their respective substrate surface unit cell (a, b, γ) and crystal orientation of the LNA. Data have been taken from reference 40. Below every 6P contact plane, the substrates on which it was reported are listed.

Enumeration	Plane	LNA	a [Å]	b [Å]	γ [°]
(a)	(001)	-	5.57	8.09	90.00
substrate		KCl (100) [67,75]; ZnO (10-10) [76]; TiO_2 (110) [77]			
(b)	(20-3)	[010]	54.60	5.57	90.00
substrate		KCl (100) [75]; TiO_2 (110) [78]; Cu (110)-(2x1)O [79]			
(c)	(11-1)	[1-10]	26.34	9.82	82.16
substrate		KCl (100) [75]; muscovite mica (001) [66,80]			
(d)	(11-2)	[1-10]	26.92	9.82	89.07
substrate		KCl (100) [75]			
(e)	(21-3)	[1-20]	26.92	13.77	94.13
substrate		TiO_2 (110) [78]; Au (111) [81]			
(f)	(-629)	[130]	54.60	18.56	82.29
substrate		Cu(110) [62,74]			

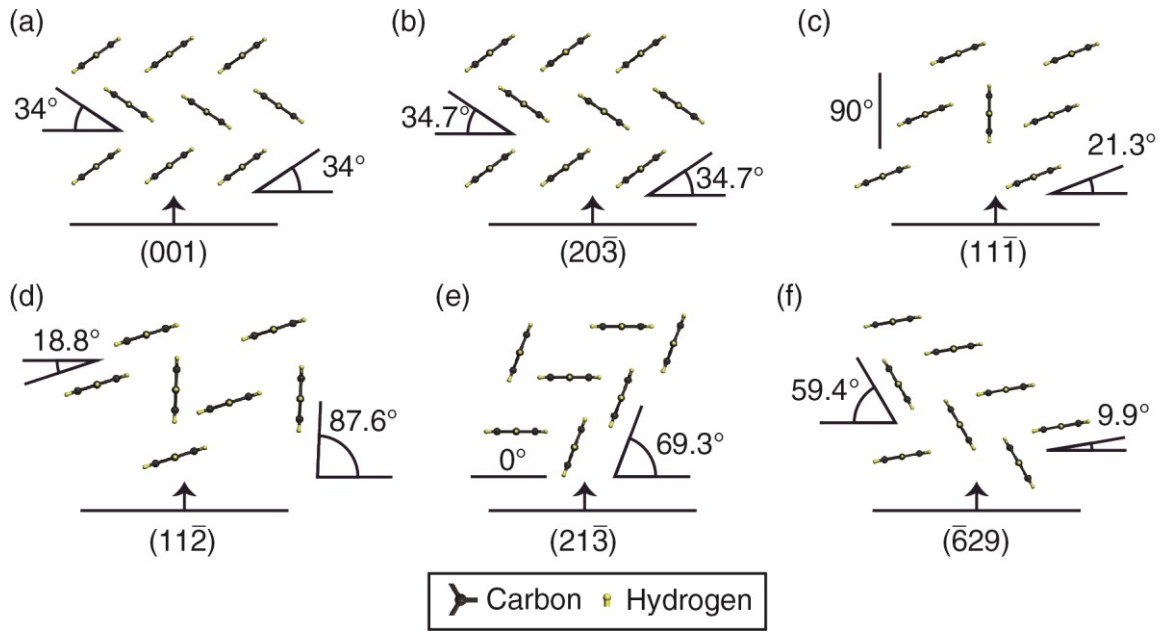

Figure 4.25: (a-f) Previously reported crystal contact planes for 6P thin films, corresponding to the enumeration in Table 4.2. Specifications of the structures have been taken from reference 40.

The question remains if any of the previously observed 6P contact planes would lead to an energetically favoured absorption position of the individual 6P molecules on top of hBN. Therefore, all 6P contact planes were projected onto the hBN (0001) substrate plane with the LNA of the 6P molecules closest to the hBN substrate fixed to an armchair direction. The only 6P contact plane where every consecutive molecule closest to the hBN substrate ended up on top of another energetically favoured adsorption site and also could describe the rotation of the 6P needle growth respective to the hBN zigzag directions was the (-629) plane. This contact plane already has been reported previously for the Cu (110) surface [62,74].

Figure 4.26 illustrates a schematic presentation of the (-629) 6P contact plane on top of the hBN substrate. If one 6P molecule closest to the substrate surface is aligned on top of the energetically most favourable adsorption site, with the centre of the phenyl rings above the nitrogen atom, every consecutive molecule will end up on top of equivalent sites. Furthermore, their phenyl ring plane is nearly parallel (only a slight tilt of 9.9°) to the hBN (0001) substrate plane. This confirms that the (-629) contact plane optimises the preferred adsorption positions of individual 6P molecules on top of the hBN substrate with the 6P crystallite bulk structure. The most important question that has to be answered is if the (-629) contact plane can also explain the rotation of the 6P needles with respect to the zigzag directions of hBN. Considering that the direction of the LNA is into the 6P [130] direction, the resulting 6P needle growth would also follow that orientation, resulting in the growth directions of the 6P needles 6.2° rotated from the zigzag directions of the hBN substrate.

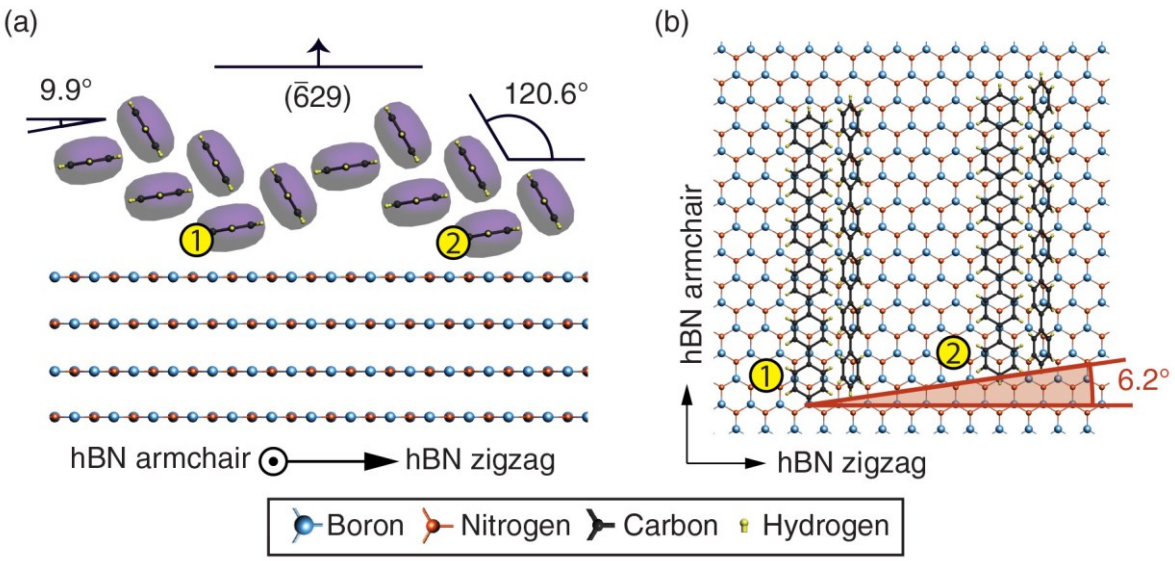

Figure 4.26: (a) Side view and (b) top view of the (-629) 6P contact plane on top of the hBN basal plane. The two molecules closest to the hBN substrate are labelled with number 1 and 2. The red angle in (b) illustrates the 6P needle growth orientation in [130] direction, exactly 6.2° off the zigzag direction [82].

In summary, the DFT calculations performed by our theory partners from Graz University and the contact plane analysis performed by Dr. A. Matković revealed, that obviously the observed six favoured growth orientations of 6P needle-like crystallites, split by ±5° of the zigzag hBN direction (Figure 4.18 and 4.19), are due to a (-629) contact plane of 6P on the hBN (0001) substrate.

5. Conclusion and Outlook

5.1. Conclusion

In this thesis, atomic force microscopy has been used to study the growth behaviour of the organic rod-like molecule 6P on top of hBN supported by an 80 nm SiO_2/Si substrate as a function of T_D and hBN flake thickness. High quality atomically thin layer hBN flakes prepared via micromechanical exfoliations were used as substrates for deposition of the 6P molecules on top of the hBN samples using the hot wall epitaxy method.

6P forms well-organized needle-like crystallites on top of the hBN surface, consisting out of flat-lying molecules maximising the sample-substrate interaction. Combined with AFM measurement analysis and DFT calculations it was possible to determine their epitaxial relation. The (-629) 6P contact plane previously observed in literature for Cu (110), results into the observed growth directions of the 6P needles ±5° rotated from a zigzag direction of the hBN, while the long axis of the individual 6P molecules is orientated along the armchair direction of the hBN substrate. With these self-assembled crystallite networks, it is possible to determine the crystallographic orientation of the underlying hBN substrate without requiring atomic resolution. In fact, the formed needle networks are large enough that it is sufficient to inspect the samples under the optical microscope. Furthermore, the 6P needles were found to overgrow hBN terraces on multilayer and bulk flakes undisturbed as long as the 6P needle height was comparable to the height of the hBN terrace. This ability could proof to be beneficial for future large scale integrations of OSC and vdW dielectrics since large-scale fabrication techniques to produce hBN flakes are usually accompanied by minor defects as cracks or terraces.

The T_D proved to have a major impact on the resulting growth morphology of the 6P needle-like crystallites. With an increase of the T_D the diffusion of the molecules on the surface is increased and the needle density is consequently reduced. Therefore, larger single crystal grains are obtained, reducing the number of grain boundaries by unit area. The highest deposition rate was found at a T_D of about 380-400 K, resulting in a network of well-ordered long 6P needle-like crystallites only limited by the size of the supporting hBN flakes.

A variation of the hBN substrate thickness also showed to influence the resulting 6P growth morphology. Below a critical thickness of 1.5 nm, 6P needles grew much shorter and did not follow preferential growth directions. This was not a direct consequence of the hBN thickness itself, but instead a combination of indirect influences arising from the hBN/SiO_2 interface, as increased hBN surface roughness, and a dipole field due to a trapped water layer beneath the

hBN flakes. To avoid these negative influences a critical hBN thickness of 1.5 nm has to be reached, which provides critical information for the use of hBN as a flexible vdW gate dielectric.

The achieved results grant a better understanding of the gate dielectric/OSC interface between hBN and 6P, therefore, allowing to control and tune the crystallite size and the level of ordering of the OSC self-assembling network at the vdW dielectric interface. This is of major importance for future OSC devices and will make them to only be limited by the intrinsic properties of the OSCs.

5.2. Outlook

The logical next step is to fabricate and examine hBN as a gate dielectric in 6P based OFETs. First attempts have already been undertaken to fabricate such devices. In collaboration with the Polymer Competence Center Leoben, aluminium was used for top and bottom contacts of hBN with shadow masks, in combination with 6P needles as the active FET layer. Top contact means that the 6P molecule is deposited before hBN is contacted and bottom contact denotes the situation where the molecules are deposited after hBN is contacted. Furthermore, in collaboration with the University of Belgrade, gold was used to top contact hBN. Another promising contact material would be graphene, enabling 2D OFETs. So far these attempts have been restricted by the limited size of the hBN flakes obtained via micromechanical exfoliation. However, the recent advances in epitaxial methods enable the fabrication of larger high-quality hBN films.

In this thesis, the growth of 6P crystallites has only been studied on top of a relaxed hBN substrate. However, in bandgap engineering strained substrates can be used to increase carrier transport in FETs. Therefore, it would be interesting to examine the growth behaviour of 6P on top of strained hBN flakes. With the help of a highly flexible polymer substrate supporting the hBN films, it might be possible to induce strain into them during the epitaxial growth process. This could lead to a completely new morphology of the 6P crystallites, possibly providing new opportunities for the tuning and ordering of the 6P crystallite network.

Furthermore, the growth of polar OSCs on top of graphene and sapphire is currently studied in a joint project together with the University Aix-Marseille. Polar molecules are expected to have much higher stability and better long-range ordering. Furthermore, they should be more sensitive to applied electrostatic fields during the epitaxial growth process, allowing to manipulate and tune them into desired structures, by externally applying electric fields.

Acknowledgments

For helping me in the course of this thesis I want to thank

Ao.Univ.-Prof. Dipl.-Phys. Dr.rer.nat. Christian Teichert for his kind and excellent supervision, for teaching me about AFM and more, for extending my view of material science, for all the travels and conferences, for giving me the opportunity to work in the SPM group and to write this thesis, providing valuable input and corrections in the process.

Dr. Aleksandar Matković for the non-replaceable input in this thesis, preparing the hBN samples, assisting me with the figures, providing the contact plane analysis, for the excellent supervision, the kind and very patient support, the correction of this thesis and good times in office and at conferences.

Dipl.-Ing. Dr.techn. Markus Kratzer for his help regarding AFM, analytical methods and the HWE system and for good times at lunch, in office and in Krakow.

Dipl.-Ing. Dr.rer.nat. Daniel Lüftner and **Assoc.-Prof. Dr. Peter Puschnig** for valuable input and the DFT calculations concerning the adsorption position of 6P on hBN.

Ing. Heinz Pirker for his technical support.

Heide Kirchberger and **Thomas Jud** for administrative support.

Dipl.-Ing. Caterina Czibula, Dipl.-Ing. Dr.mont. Christian Ganser, Kevin Gradwohl, Dipl.-Ing Michael Lasnik, Dipl.-Ing. Stefan Klima, Michael Huszar, Msc Benjamin Kaufmann, Mag.inz. Monika Mirkowska, Dipl.-Ing. Patrice Kreiml and **Dipl.-Ing. Quan Shen** for the excellent working atmosphere and good times in office and at conferences.

The Austrian Science Fund (FWF) for financial support.

My whole IBC Leoben team for providing me sporting balance during my studies and countless hours of entertainment.

All of my family, especially my brother Martin and my parents

My friends and colleagues

6. Bibliography

[1] K. S. Novoselov, A. K. Geim, S. V. Morozov, D. Jiang, Y. Zhang, S. V. Dubonos, I. V. Grigorieva, and A. A. Firsov. Electric Field Effect in Atomically Thin Carbon Films. *Science* **306**, 666–669 (2004).

[2] K. Geim and I. V. Grigorieva. Van der Waals heterostructures. *Nature* **499**, 419–425 (2013).

[3] A. A. Balandin. Thermal properties of graphene and nanostructured carbon materials. *Nature Materials* **10**, 569-581 (2011).

[4] M. Osada and T. Sasaki. Two-Dimensional Dielectric Nanosheets: Novel Nanoelectronics From Nanocrystal Building Blocks. *Advanced Materials* **24**, 210–228 (2012).

[5] C. W. Chang, D. Okawa, A. Majumdar and A. Zettl. Solid-State Thermal Rectifier. *Science* **314** (2006), 1121-1124.

[6] D. Goldberg, P. M. F. J. Costa, O. Lourie, M. Mitome, X. Bai, K. Kurashima, C. Zhi. C. Tank and Y. Bando. Direct Force Measurements and Kinking under Elastic Deformation of Individual Multiwalled Boron Nitride Nanotubes. *Nano Letters* **7**, 2146-2151 (2007).

[7] N. Kostoglou, K. Polychronopoulou and C. Rebholz. Thermal and chemical stability of hexagonal boron nitride (h-BN) nanoplatelets. *Vacuum* **112**, 42-45 (2015).

[8] H. O. Pierson. Boron Nitride Composites By Chemical Vapor Deposition. *Journal of Composite Materials* **9**, 228-240 (1975).

[9] J. Bao, K. Jeppson, M. Edwards, Y. Fu, L. Ye, X. Lu, and Johan Liu. Synthesis and applications of two-dimensional hexagonal boron nitride in electronics manufacturing. *Electronic Materials Letters* **12**, 1-16 (2016).

[10] Y. Zhang. Probing carrier transport and structure-property relationship of highly ordered organic semiconductors at the two-dimensional limit. *Physical Review Letters* **116**, 016602 (2016).

[11] C-a. Di, D. Wei, G. Yu, Y. Liu, Y. Guo and D. Zhu. Patterned graphene as source/drain electrodes for bottom-contact organic field-effect transistors. *Advanced Materials* **20**, 3289–3293 (2008).

[12] G. Hlawacek, F. S. Khokhar, R. van Gastel, B. Poelsema and C. Teichert. Smooth growth of organic semiconductor films on graphene for high-efficiency electronics. *Nano Letters* **11**, 333–337 (2011).

[13] G.-H. Lee, C.-H. Lee, A. M. van der Zande, M. Han, X. Ciu, G. Arefe, C. Nuckolls, T. F. Heinz, J. Hone and P. Kim. Heterostructures based on inorganic and organic van der Waals systems. *Applied Materials* **2**, 092511 (2014).

[14] C.-H. Lee, T. Schiros, E. J. G. Santos, B. Kim, K. G. Yager, S.J. Kang, S. Lee, J. Yu, K. Watanabe and T. Taniguchi. Epitaxial growth of molecular crystals on van der waals substrates for high-performance organic electronics. *Advanced Materials* **26**, 2812–2817 (2014).

[15] D. Jariwala, S. L. Howell, K. S. Chen, J. Kang, V. K. Sangwan, S. A. Filippone, R. Turrisi, T. J. Marks, L. J. Lauhon and M. C. Hersam. Hybrid, Gate-Tunable, van der Waals p-n heterojunctions from Pentacene and MoS_2. *Nano Letters* (2016).

[16] M. Kratzer and C. Teichert. Thin film growth of aromatic rod-like molecules on graphene. *Nanotechnology* **27**, 292001 (2016).

[17] Y. D. Park, J. A. Lim, H. S. Lee and K. Cho. Interface engineering in organic transistors. *Materials Today* **10**, 46–54 (2007).

[18] C-a. Di, Y. Liu, G. Yu and D. Zhu. Interface Engineering: An Effective Approach toward High. Performance Organic Field-Effect Transistors. *Accounts of Chemical Research* **42**, 1573–1583 (2009).

[19] R. Ruiz, A. Papadimitratos, A. C. Mayer and G. G. Malliaras. Thickness Dependence of Mobility in Pentacene Thin-Film Transistors. *Advanced Materials* **17**, 1795–1798 (2005).

[20] F. Dinelli, M. Murgia, P. Levy, M. Cavallini, F. Biscarini and D. M. de Leeuw. Spatially correlated charge transport in organic thin film transistors. *Physical Review Letters* **92**, 116802 (2004).

[21] A. v. Mühlenen, M. Castellani, M. Schaer and L. Zuppiroli. Controlling charge-transfer at the gate interface of organic field-effect transistors. *Physica Status Solidi (b)* **245**, 1170–1174 (2008).

[22] D. Kumaki, M. Yahiro, Y. Inoue and S. Tokito. Air stable, high performance pentacene thin-film transistor fabricated on sio2 gate insulator treated with beta-phenethyltrichlorosilane. *Applied Physics Letters* **90**, 133511 (2007).

[23] Y. Wen, Y. Liu, C.-a. Di, Y. Wang, X. Sun, Y. Guo, J. Zheng, W. Wu, S. Ye and G. Yu. Improvements in Stability and Performance of N,N'-Dialkyl Perylene Diimide-Based n-Type Thin-Film Transistors. *Advanced Materials* **21**, 1631–1635 (2009).

[24] C-a. Di, G. Yu, Y. Liu, Y. Guo, X. Sun, J. Zheng, Y. Wen, Y. Wang, W. Wu and D. Zhu. Effect of dielectric layers on device stability of pentacene-based field-effect transistors. *Physical Chemistry Chemical Physics* **11**, 7268–7273 (2009).

[25] S. Steudel, S. D. Vusser, S. D. Jonge, D. Janssen, S. Verlaak, J. Genoe and P. Heremans. Influence of the dielectric roughness on the performance of pentacene transistors. *Applied Physics Letters* **85**, 4400–4402 (2004).

[26] J. Veres, S. Ogier and G. Lloyd. Gate insulators in organic field-effect transistors. *Chemistry of Materials* **16**, 4543–4555 (2004).

[27] A. Koma. Van der Waals epitaxy for highly lattice-mismatched systems. *Journal of Crystal Growth* **201**, 236–241 (1999).

[28] B. Liam, R. V. Gorbachev, R. Jalil, B. D. Belle, F. Schedin, M. I. Katsnelson, L. Eaves, S. V. Morozov, A. S. Mayorov, N. M. R. Peres, A. H. Castro Neto, J. Leist, A. K. Geim, L. A. Ponomarenko and K. S. Novoselov. Electron tunnelling through ultrathin boron nitride crystalline barriers. *Nano Letters* **12**, 1707–1710 (2012).

[29] A. Mishchenko, Y. Cao, G. L. Yu, C. R. Woods, R. V. Gorbachev, K. S. Nososelov, A. K. Geim and L. S. Levitov. Nonlocal response and anamorphosis: The case of few-layer black phosphorus. *Nano Letters* **15**, 6991–6995 (2015).

[30] Y. Cao, A. Mishchenko, G. L. Yu, E. Khestanova, A. P. Rooney, E. Prestat, A. V. Kretinin, P. Blake, M. B. Shalom, C. Woods, J. Chapman, G. Balakrishnan, I. V. Grigorieva, K. S. Novoselov, B. A. Pilot, M. Potemski, K. Watanabe, T. Taniguchi, S. J. Haigh, A. K. Geim and R. V. Gorbachev. Quality heterostructures from two-dimensional crystals unstable in air by their assembly in inert atmosphere. *Nano Letters* **15**, 4914–4921 (2015).

[31] D. Goldberg, Y. Bando, Y. Huang, T. Terao, M. Mitome, C. Tang and C. Zhi. Boron nitride nanotubes and nanosheets. *ACS Nano* **4**, 2979-2993 (2010).

[32] Y. Wang, Z. Shi, and J. Yin. Boron nitride nanosheets: Large-scale exfoliation in methanesulfonic acid and their composites with polybenzimidazole. *Journal of Materials Chemistry* **21**, 11371 (2011).

[33] R. Decker, Y. Wang, V. W. Brar, W. Regan, H.-Z. Tsai, Q. Wu, W. Gannett, A. Zettl and M. F. Crommie. Local Electronic Properties of Graphene on a BN Substrate via Scanning Tunneling Microscopy. *Nano Letters* **11**, 2291–2295 (2011).

[34] S. Caneva, R. S. Weatherup, B. C. Bayer, B. Brennan, S. J. Spencer, K. Mingard, A. Cabrero-Vilatela, C. Baehtz, A. J. Pollard and S. Hofmann. Nucleation for Large, Single Crystalline Domains of Monolayer Hexagonal Boron Nitride via Si-Doped Fe Catalyst. *Nano Letters* **15**, 1867-1875 (2015)

[35] K. Watanabe, T. Taniguchi and H. Kanda. Direct-bandgap properties and evidence for ultraviolet lasing of hexagonal boron nitride single crystal. *Nature Materials* **3**, 404–409 (2004).

[36] T. Taniguchi and K. Watanabe. Synthesis of high-purity boron nitride single crystals under high pressure by using Ba–BN solvent. *Journal of Crystal Growth* **303**, 525–529 (2007).

[37] K. S. Novoselov, D. Jiang, F. Schedin, T. J. Booth, V. V. Khotkevich, S. V. Morozov and A. K. Geim. Two-dimensional atomic crystals. *Proceedings of the National Academy of Sciences of the United States of America* **102**, 10451–10453 (2005).

[38] A. K. Geim and I. V. Grigorieva. Van der waals heterostructures. *Nature* **499**, 419–425 (2013).

[39] K. N. Baker, A. V. Fratini, T. Resch, H. C. Knachel and W. W. Adams. Crystal structures, phase transitions and energy calculations of poly(p-phenylene) oligomers. *Polymer* **34**, 1571-1587 (1993).

[40] C. Simbrunner. Epitaxial growth of sexi-thiophene and para-hexaphenyl and its implications for the fabrication of self-assembled lasing nano-fibres. *Semiconductor Science and Technology* **28**, 053001 (2013).

[41] A. Lopez-Otero. Hot wall epitaxy. *Thin Solid Films* **49**, 3–57 (1978).

[42] H. Sitter, A. Andreev, G. Matt and N. S. Sariciftci. Hot-wall-epitaxy – the method of choice for the growth of highly ordered organic epilayers. *Molecular Crystals and Liquid Crystals* **385**, 51-60 (2002).

[43] M. Kratzer, S. Klima, C. Teichert, B. Vasic, A. Matcovic, M. Milicevic and R. Gajic. Layer Dependent Wetting in Parahexaphenyl Thin Film Growth on Graphene. *e-Journal of Surface Science and Nanotechnology* **12**, 31–39 (2014).

[44] M. Kratzer, S. Klima, C. Teichert, B. Vasic, A. Matcovic, U. Ralevic and R. Gajic. Temperature dependent growth morphologies of parahexaphenyl on SiO_2 supported exfoliated graphene. *Journal of Vacuum Science & Technology B* **31**, 04D114 (2013).

[45] R. Haubner, M. Wilhelm, R. Weissenbacher and B. Lux. Boron Nitrides – Properties, Synthesis and Applications. *High Performance Non-Oxide Ceramics II* **102**, 1-45 (2002).

[46] G. Constantinescu, A. Kuc and T. Heine. Stacking in Bulk and Bilayer Hexagonal Boron Nitride. *Physical Review Letters* **111**, 036104 (2013).

[47] R. V. Gorbachev, I. Riaz, R. R. Nair, R. Jalil, L. Britnell, B. D. Belle, E. W. Hill, K. S. Novoselov, K. Watanabe, T. Taniguchi, A. K. Geim and P. Blake. Hunting for Monolayer Boron Nitride: Optical and Raman Signatures. *Small* **7**, 465-468 (2011).

[48] G. Giovannetti, P. A. Khomyakov, G. Brocks, P. J. Kelly and J. van den Brink. *Physical Review B* **76**, 073103 (2007).

[49] C. R. Dean, A. F. Young, I. Meric, C. Lee, L. Wang, S. Sorgenfrei, K. Watanabe, T. Taniguchi, P. Kim, K. L. Shepard and J. Hone. Boron nitride substrates for high-quality graphene electronics. *Nature Nanotechnology* **5**, 722-726 (2010).

[50] P. Puschnig and C. Ambrosch-Draxl. Density-functional study for the oligomers of poly(para-phenylene): Band structures and dielectric tensors. *Physical Review B* **60**, 7891 (1999).

[51] H. Yanagi and T. Morikawa. Self-waveguided blue light emission in p-sexyphenyl crystals epitaxially grown by mask-shadowing vapor deposition. *Applied Physics Letters* **75**, 187 (1999).

[52] C. C. Jensen and H. Schroder. Complete optical analysis of an UV laser dye using saturation techniques. *Applied Optics* **31**, 7012-7021 (1992).

[53] H. O. Marcy, M. J. Rosker, L. F. Warren, B. A. Reinhardt, M. Sinclair and C. H. Seager. Time-resolved degenerate four-wave mixing studies of solid-state poly(p-phenylene) oligomers. *The Journal of Chemical Physics* **100**, 3325 (1994).

[54] F. Quochi, F. Cordella, A. Mura and G. Bongiovanni. One-Dimensional Random Lasing in a single Organic Nanofiber. *The Journal of Physical Chemistry B* **109**, 21690-21693 (2005).

[55] R. Resel. Crystallographic studies on hexaphenyl thin films – a review. *Thin Solid Films* **433**, 1-11 (2003).

[56] G. Binning, C. F. Quate and C. Gerber. Atomic force microscope. *Physical Review Letters* **56**, 930 (1986).

[57] P. Eaton and P. West. Atomic force Microscopy. *Oxford: Oxford University Press* (2010).

[58] A. V. Matković. Investigating the optical properties of graphene with spectroscopic ellipsometry. PhD Thesis, University of Belgrade 2015.

[59] D. Necas and P. Klapetek. Gwyddion: an open-source software for SPM data analysis. *Open Physics* **10**, 181-188 (2012).

[60] Asylum Research Probe Store. [Online]. Available: http://www.asylumresearch.com/ProbeStore. [Accessed: October 2016].

[61] Gwyddion Documentation. [Online]. Available: http://www.gwyddion.net. [Accessed September 2016]

[62] A. J. Fleming, S. Berkebile, T. Ules and M. G. Ramsey. Pre-nucleation dynamics of organic molecule self-assembly investigated by PEEM. *Physical Chemistry Chemical Physics* **13**, 4693-4708 (2011).

[63] C. K. Oliveira, M. J. S. Matos, M. S. C. Mazzoni, H. Chacham and B. R. A. Neves. Anomalous response of supported few-layer hexagonal boron nitride to DC electric fields: a confined water effect? *Nanotechnology* **23**, 175703 (2012).

[64] L. Chen, X. Yu and D. Wang. Cantilever dynamics and quality factor control in AC mode AFM height measurements. *Ultramicroscopy* **107**, 275-280 (2007).

[65] S. Lorbek, G. Hlawacek and C. Teichert. Determination of critical island size in para-sexiphenyl islands on SiO2 using capture-zone scaling. *The European Physical Journal Applied Physics* **55**, 23902 (2011).

[66] F. Balzer, M. Schiek, H-G Rubahn, K. Al-Shamery and A. Lutzen. Surface bound organic nanowires. *Journal of Vacuum Science and Technology B* **26**, 1619 (2008).

[67] H. Yanagi, T. Ohara and T. Morikawa. Self-Waveguided Gain-Narrowing of Blue Light Emission form Epitaxially Oriented p-Sexiphenyl Crystals. *Advanced Materials* **13,** 1452-1455 (2001).

[68] G. Hlawacek, P. Puschnig, P. Frank, A. Winkler, C. Ambrosch-Draxl, C. Teichert. Characterization of Step-Edge Barriers in Organic Thin-Film Growth. *Science* **321**, 108-111 (2008).

[69] P. Frank, G. Hlawacek, O. Lengyel, A. Satka, C. Teichert, R. Resel, A. Winkler. Influence of surface temperature and surface modifications on the initial layer growth of para-hexaphenyl on mica (001). *Surface Science* **601**, 2152-2160 (2007).

[70] J. A. Venables, G. D. T. Spiller and M. Hanbücken. Nucleation and growth of thin films. *Reports on Progress in Physics* **47**, 399-459 (1984)

[71] S. S. Datta, D. R. Strachan, E. J. Mele, and A. T. C. Johnson. Surface Potentials and Layer Charge Distributions in Few-Layer Graphene Films. *Nano Letters* **9**, 7-11 (2009).

[72] A. Castellanos-Gomez, E. Cappelluti, R. Rolan, N. Agrait, F. Guinea, G. Rubio-Bollinger. Electric-Field Screening in Atomically Thin Layers of MoS_2: the Role of Interlayer Coupling. *Advanced Materials* **25**, 899-903 (2013).

[73] L. H. Li, E. J. G. Santos, T. Xing, E. Cappelluti, R. Roldan, Y. Chen, K. Watanabe and T. Taniguchi. Dielectric Screening in Atomically Thin Boron Nitride Nanosheets. *Nano Letters* **15**, 218-223 (2015).

[74] J. Novak, M. Oehzelt, S. Berkebile, M. Koini, T. Ules, G. Koller, T. Haber, R. Resel and M. G. Ramsey. Crystal growth of para-sexiphenyl on clean and oxygen reconstructed Cu(110) surfaces. *Physical Chemistry Chemical Physics* **13**, 14675-14684 (2011).

[75] T. Haber, M. Oehzelt, R. Resel, A. Andreev, A. Thierry, H. Sitter, D.-M- Smilgies, B. Schaffer, W. Grogger and R. Wesel. Single Crystalline Nature of para-Sexiphenyl Crystallites Grown on KCl(100). *Journal of Nanoscience and Nanotechnology* **6**, 698-703 (2006).

[76] M. Sparenberg, A. Zykov, P. Beyer, L. Pithan, C. Weber, Y. Garmshausen, F. Carla, S. Hecht, S. Blumstengel, F. Henneberger and S. Kowarik. Controlling the growth of para-sexiphenyl (6P) on ZnO by partial fluorination. *Physical Chemistry Chemical Physics* **16**, 26084-26093 (2014).

[77] G. Koller, S. Berkebile, R. J. Krenn, F. P. Netzer, M. Oehzelt, T. Haber, R. Resel and M. G. Ramsey. Heteroepitaxy of Organic-Organic Nanostructures. *Nano Letters* **6**, 1207-1212 (2006).

[78] R. Resel, M. Oehzelt, O. Lengyel, T. Haber, T. U. Schulli, A. Thierry, G. Hlawacek, C. Teichert, S. Berkebile, G. Koller and M. G. Ramsey. The epitaxial sexiphenyl (001) monolayer on TiO_2(110): A grazing incidence X-ray diffraction study. *Surface Science* **19**, 4645-4649 (2006).

[79] M. Oehzelt, L. Grill, S. Berkebile, G. Koller, F. P. Netzer and M. G. Ramsey. The Molecular Orientation of para-Sexiphenyl on Cu(110) and Cu(110) p(2x1)O. *ChemPhysChem* **8**, 1707-1712 (2007).

[80] T. Djuric, G. Hernandez-Sosa, G. Schwabegger, M. Koini, G. Hesser, M. Arndt, M. Brinkmann, H. Sitter, C. Simbrunner and Roland Resel. Alternately deposited heterostructures of α-sexithiophene-para-hexaphenyl on muscovite mica(001) surfaces: crystallographic structure and morphology. *Journal of Materials Chemistry* **22**, 15316 (2012).

[81] T. Haber, S. Muelleger, A. Winkler and R. Resel. Temperature-induced epitaxial growth modes of para-sexiphenyl on Au(111). *Physical Review B* **74**, 045419 (2006).

[82] A. Matković, J. Genser, D. Lüftner, M. Kratzer, R. Gajić, P. Puschnig and C. Teichert. Epitaxy of highly ordered conjugated organic semiconductor crystallite networks supported by hexagonal boron nitride. *Scientific Reports* **6**, 38519-1-10 (2016).